Accepted Manuscript

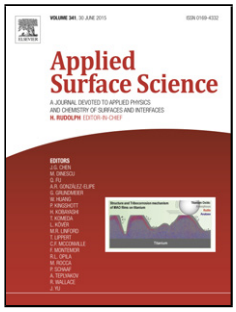

Title: Structural, photoluminescent and photocatalytic properties of TiO_2:Eu^{3+} coatings formed by plasma electrolytic oxidation

Author: Stevan Stojadinović Nenad Radić Boško Grbić Slavica Maletić Plamen Stefanov Aleksandar Pačevski Rastko Vasilić

PII: S0169-4332(16)30309-9
DOI: http://dx.doi.org/doi:10.1016/j.apsusc.2016.02.131
Reference: APSUSC 32649

To appear in: *APSUSC*

Received date: 24-12-2015
Revised date: 9-2-2016
Accepted date: 13-2-2016

Please cite this article as: S. Stojadinović, N. Radić, B. Grbić, S. Maletić, P. Stefanov, A. Pačevski, R. Vasilić, Structural, photoluminescent and photocatalytic properties of TiO_2:Eu^{3+} coatings formed by plasma electrolytic oxidation, *Applied Surface Science* (2016), http://dx.doi.org/10.1016/j.apsusc.2016.02.131

Structural, photoluminescent and photocatalytic properties of $TiO_2:Eu^{3+}$ coatings formed by plasma electrolytic oxidation

Stevan Stojadinović[a*], Nenad Radić[b], Boško Grbić[b], Slavica Maletić[a], Plamen Stefanov[c], Aleksandar Pačevski[d], Rastko Vasilić[a]

[a] *University of Belgrade, Faculty of Physics, Studentski trg 12-16, 11000 Belgrade, Serbia*

[b] *University of Belgrade, Institute of Chemistry, Technology and Metallurgy, Department of Catalysis and Chemical Engineering, Njegoševa 12, 11000 Belgrade, Serbia*

[c] *Institute of General and Inorganic Chemistry, Bulgarian Academy of Sciences, Acad. G. Bonchev Str., Block 11, 1113 Sofia, Bulgaria*

[d] *University of Belgrade, Faculty of Mining and Geology, Đušina 7, 11000 Belgrade, Serbia*

*Corresponding author. Tel: + 381-11-7158161; Fax: + 381-11-3282619

E-mail address: sstevan@ff.bg.ac.rs (Stevan Stojadinović)

Abstract

In this paper, we used plasma electrolytic oxidation (PEO) of titanium in water solution containing 10 g/L $Na_3PO_4 \cdot 12H_2O$ + 2 g/L Eu_2O_3 powder for preparation of $TiO_2:Eu^{3+}$ coatings. The surfaces of obtained coatings exhibit a typical PEO porous structure. The energy dispersive x-ray spectroscopy analysis showed that the coatings are mainly composed of Ti, O, P, and Eu; it is observed that Eu content in the coatings increases with PEO time. The x-ray diffraction analysis indicated that the coatings are crystallized and composed of anatase and rutile TiO_2 phases, with anatase being the dominant one. X-ray photoelectron spectroscopy revealed that Ti 2p spin-orbit components of $TiO_2:Eu^{3+}$ coatings are shifted towards higher binding energy, with respect to pure TiO_2 coatings, suggesting that Eu^{3+} ions are incorporated into TiO_2 lattice. Diffuse reflectance spectroscopy showed that $TiO_2:Eu^{3+}$ coatings exhibit evident red shift with respect to the pure TiO_2 coatings. Photoluminescence

(PL) emission spectra of TiO_2:Eu^{3+} coatings are characterized by sharp emission bands in orange-red region ascribed to f–f transitions of Eu^{3+} ions from excited level $^5D_0$ to lower levels ^7F_J (J = 0, 1, 2, 3, and 4). The excitation PL spectra of TiO_2:Eu^{3+} coatings can be divided into two regions: the broad band region from 250 nm to 350 nm associated with charge transfer state of Eu^{3+} and the series of sharp peaks in the range from 350 nm to 550 nm corresponding to direct excitation of the Eu^{3+} ions. It is observed that the intensity of peaks in excitation and emission PL spectra increases with the concentration of Eu^{3+}, but the peak positions remain practically unchanged. The ratio of PL emission for electric and magnetic dipole transitions indicates highly asymmetric environment around Eu^{3+} ions. The photocatalytic activity (PA) of TiO_2:Eu^{3+} coatings is evaluated by measuring the photodegradation of methyl orange under simulated sunlight conditions. It is shown that PEO time, i.e., the amount of Eu^{3+} incorporated into coatings is an important factor affecting PA; TiO_2:Eu^{3+} coating formed after 1 min of PEO time showed the highest PA.

Keywords: Plasma electrolytic oxidation (PEO), TiO_2; Eu^{3+}; Photoluminescence; Photocatalysis;

1. Introduction

Titanium dioxide (TiO_2) has been widely studied in the last few decades because of its potential applications including photocatalysis, structural ceramics, dye-sensitized solar cells, sensors, biocompatible materials, etc. [1-5]. Many efforts have been made to explore TiO_2 based phosphors doped with various rare earth ions as luminescence materials, because of their excellent luminescence characteristics with sharp emission bands originating from the electronic transition between f levels [6-12]. Also, doping of TiO_2 with rare earth ions proved to be an efficient method to improve the photocatalytic properties of TiO_2. The enhancement of the photocatalytic activity of rare earth doped TiO_2 has been ascribed to a combination of

several factors: (i) the formation of oxygen vacancy charge trapping centers leading to a decrease of electron/hole recombination rate; (ii) extending the response of TiO_2 into the visible region; (iii) increasing the anatase to rutile transformation temperature, and (iv) pollutant interaction with rare earth metals doped into TiO_2 via f-orbitals increase its ability to absorb the pollutant molecules and enhance the photocatalytic efficiency [13-21].

In recent years, Eu^{3+} doped TiO_2 has attracted much attention because of its use as a luminescent material in orange-red visible region and as an efficient photocatalyst. Many techniques such as precipitation method [21], pulsed-laser deposition [22], spray pyrolysis [23], sol-gel method [24], hydrothermal method [25], thermal plasma pyrolysis [26], etc. have been employed for the formation of the Eu^{3+} doped TiO_2. In this paper, we have applied plasma electrolytic oxidation process for the synthesis of TiO_2:Eu^{3+} coatings.

Plasma electrolytic oxidation (PEO) is an economic, efficient, and environmentally benign processing [27-29]. During the PEO process discrete spark discharges occur on the coating's surface when applied voltage is higher than a critical value (known as the breakdown voltage). Discharge characteristics, both individual and collective, determine thermal and chemical conditions on the oxidizing surface and play an important role in the phase formation and structure of the oxide coatings. Oxide coatings formed by PEO usually contain crystalline and amorphous phases where constituent species can originate both from metal and electrolyte.

Recently, a lot of research has been focused on the preparation of TiO_2 photocatalysts obtained by PEO of titanium and titanium alloys in different electrolytes. Research efforts have been directed towards improving visible light absorption and reducing electron/hole recombination rate of such coatings by coupling TiO_2 with narrow band gap semiconducting materials and metallic and non-metallic species [30-32]. The main advantage of using PEO in producing TiO_2 based photocatalysts is very short fabrication time caused by skipping the

annealing step, which is required to transform amorphous TiO_2 into its crystalline phase(s). Also, TiO_2 coatings formed by PEO on titanium substrate have excellent adhesion and anti-corrosion performance which is highly desirable for industrial applications.

Up to now, a vast number of TiO_2:Eu^{3+} photocatalytic studies has been directed towards utilizing TiO_2 nanocrystalline powders [21,24,33-35]. The drawback of such systems is the necessity of filtration of the powder photocatalyst from treated effluent after the treatment, which makes the process difficult, time consuming, and expensive. On the other hand, with immobilizing TiO_2:Eu^{3+} these limitations can be overcome. The aim of this work was to examine the possibility of formation of TiO_2:Eu^{3+} coatings on titanium substrate by PEO in supporting electrolyte containing Eu_2O_3 powder and to probe their photoluminescent and photocatalytic properties. Scanning electron microscopy, X-ray energy dispersive spectroscopy, X-ray diffraction, X-ray photoelectron spectroscopy, PL spectral measurements, and diffuse reflectance spectroscopy were used as tools to characterize formed TiO_2:Eu^{3+} coatings.

2. Experimental details

Titanium samples (99.5% purity, Alfa Aesar) of dimensions 25 mm × 10 mm × 0.25 mm were used as working electrode in the experiment. The working electrodes were sealed with insulation resin leaving only active surface with an area of 15 mm × 10 mm accessible to the electrolyte. Schematic diagram of the experimental setup used for PEO is shown in Fig. 1. PEO process was carried out in a Pyrex beaker of 500 mL capacity. The titanium samples and two platinum plates of dimensions 40 mm x 20 mm were used as the anode and cathodes in the experiment, respectively. The electrodes were in parallel alignment and the distance between the anode and each of the cathodes was 2 cm. During the PEO, current density was set to 150 mA/cm^2. The power supply was a Consort EV261 DC power unit providing

voltages 0–600 V and a current of 0–1000 mA. Water solution of 10 g/L sodium phosphate dodecahydrate ($Na_3PO_4 \cdot 12H_2O$) was used as a supporting electrolyte. Commercially available Eu_2O_3 powder was added to supporting electrolyte in the concentration of 2 g/L. The pH of the electrolyte at working conditions was 12.2 while the conductivity was 7.9 mS/cm. During the PEO, the electrolyte was stirred with a magnetic stirrer to ensure the homogenous distribution of particles in the electrolyte and circulated through the chamber–reservoir system. The temperature of the electrolyte was maintained during the PEO at (20 ± 1) ºC. After the PEO, samples were rinsed in distilled water to prevent additional deposition of electrolyte components during drying.

Scanning electron microscope (SEM) JSM 6610LV equipped with an INCA 350 energy dispersion X-ray (EDS) analysis was used to characterize the morphology and chemical composition of formed coatings. The crystallinity of formed coatings was analyzed by X-ray diffraction (XRD), using a Rigaku Ultima IV diffractometer in Bragg–Brentano geometry, with Ni filtered CuKα radiation (λ=1.54178 Å). Diffraction data were acquired over the scattering angle 2θ from 20° to 60° with a step of 0.020° and acquisition rate of 2°/min. The x-ray photoelectron spectra (XPS) were acquired on a Kratos AXIS Supra photoelectron spectrometer using a monochromatic Al Kα source with energy of 1486.6 eV. The base pressure in the analysis chamber was $5 \cdot 10^{-8}$ Pa. Binding energies were corrected relative to the C 1s signal at 285.0 eV.

PL spectral measurements were taken on a Horiba Jobin Yvon Fluorolog FL3-22 spectrofluorometer at room temperature, with a 450 W xenon lamp as the excitation light

source. The obtained spectra were corrected for the spectral response of the measuring system and spectral distribution of the Xe lamp. UV–Vis diffuse reflectance spectra (DRS) of formed coatings were recorded using a UV–Vis spectrophotometer (Shimadzu UV-3600).

Photocatalytic activity of formed coatings was investigated by photodegrading methyl orange (MO) at room temperature. Samples with an area of 1.5 cm^2 were dipped into 10 mL of 8 mg/L aqueous MO solution. Catalyst foil in the photocatalytic reactor was placed on perforated holder, 5 mm above the bottom of the reactor, with magnetic stirrer under the holder. Prior to illumination, the solution and the catalyst were magnetically stirred in the dark for 30 min to achieve adsorption–desorption equilibrium. MO solution was then irradiated under the lamp that simulates solar radiation (Solimed BH Quarzlampen), with a power consumption of 300 W. The light source was set at distance of 25 cm above the top surface of the solution. A fixed quantity of the MO solution was removed every 2 hours to measure the absorption and then concentration, using UV-Vis spectrometer (Thermo Electron Nicolet Evolution 500). After each measurement of MO concentration probe solution was returned back to the photocatalytic reactor. MO has a maximum absorbance at 464 nm, which was used as a wavelength for monitoring MO degradation. The absorbance was converted to MO concentration in accordance with standard curve showing a linear relationship between the concentration and the absorbance at this wavelength. Prior to the photocatalysis, MO solution was tested for photolysis in the absence of the photocatalyst in order to examine its stability. The lack of change in the MO concentration after 12 h of irradiation revealed that the MO was stable under applied conditions and that degradation was only due to the presence of the photocatalyst.

3. Results and discussion

3.1. Morphology, chemical and phase composition of TiO_2:Eu^{3+} coatings

Typical voltage–time curve during the anodization of titanium in 10 g/L $Na_3PO_4 \cdot 12H_2O$ + 2 g/L Eu_2O_3 at constant current density of 150 mA/cm^2 is shown in Fig. 2a.

A linear increase of the voltage in region I is related to relatively uniform growth of a compact oxide layer. In this region oxide layer grows at the titanium/oxide and oxide/electrolyte interfaces as a result of migration of O^{2-}/OH^- and Ti^{4+} ions across the oxide assisted by a strong electric field (~10^7 V/cm) [36]. Also, small amounts of anionic components of electrolyte are incorporated into the coating at the oxide/electrolyte interface. Initial oxide layer forms at the surface of titanium as a result of the following overall reaction:

$$Ti + 2H_2O \rightarrow TiO_2 + 4H^+ + 4e^- \quad (1)$$

At the potential of about 265 V uniform film thickening is terminated by dielectric breakdown (beginning of PEO process) and voltage-time curve deflects from linearity. In region II a large number of small discharges are visible. Further anodization results in relatively stable value of the voltage while discharging continues (region III). During PEO various plasma-chemical, electrochemical, and thermodynamical processes are induced at the discharge sites due to high plasma temperature and pressure [37]. These processes are modifying the morphology, structure and composition of the formed coatings. SEM micrographs of the surface coatings formed at various stages of PEO process are shown in

Fig. 2b. A number of discharge channels and regions resulting from the rapid cooling of molten material are present on the surface (Fig. 2b). At the discharge sites local temperature sharply increases to about 10^4 K [38], high enough to melt the oxide coating. Due to the strong electric field, anionic components of electrolyte are drawn into these channels. Transfer of Eu_2O_3 particles towards the titanium substrate is also possible in the strong electric fields inherent to plasma discharging and it is further promoted by hydrodynamic effects caused by titanium surface heating and convection [21]. Concurrently, the titanium substrate is melted out through discharge channels and gets oxidized. Eu_2O_3 particles melt inside the discharge channels, because their melting point (~2620 K) is much lower than the plasma electron temperature during PEO [39]. Molten Eu_2O_3 particles react with other components from the electrolyte and the substrate to form mixed-oxide coatings. After the short-living discharging, the molten regions quench in contact with the surrounding electrolyte, leading to the formation of solidified molten oxides composed of both titanium and materials originating from the electrolyte. By the repetition of this process at a number of discrete locations over the coating surface, the thickness of the coating increases. Fig. 2c shows backscattered SEM micrographs of polished cross-sections of PEO coatings grown on titanium from electrolyte containing Eu_2O_3 powder. Throughout the PEO process, the average coating thickness increases at the rate of approximately 1.5 μm/min (Fig. 1a). The coatings show porous microstructure which is typical for coatings formed by PEO. Results of the EDS analyses of surface coatings in Fig. 2b are shown in Table 1. Main elements of the coatings are Ti, P, O, and Eu. The concentration of Eu increases with PEO time. In order to investigate the distribution of Ti, P, O, and Eu in the coatings formed by PEO, EDS elemental mapping was carried out (Fig. 3). All elements are uniformly distributed in the coating, but some areas with high agglomeration of Eu were be observed.

The XRD patterns of TiO_2:Eu^{3+} coatings formed after various PEO times are shown in Fig. 4a. Diffraction peaks corresponding to anatase phase (A) of TiO_2 (PDXL DB Card No. 9008213) and rutile phase (R) of TiO_2 (PDXL DB Card No. 9009083) can be observed in XRD patterns. Elemental Ti originates from the substrate due to penetration of X-rays through the porous surface layer and reaching the substrate. XRD patters of pure TiO_2 coatings are quite similar to XRD patterns of TiO2:Eu^{3+}coatings formed under the same conditions as in Fig. 4a, so we have decided to omit them. XRD pattern of pure Eu_2O_3 powder used in this research is shown in Fig. 4b. The peaks are in accordance with the typical cubic type structure of Eu_2O_3 crystals. We were not able to detect any peaks corresponding to europium species in XRD patterns of obtained coatings. The main reason for this is the low concentration of Eu_2O_3 particles all over the coatings' surface. Also, the incorporation of a small quantity of Eu^{3+} ions from the electrolyte into TiO_2 coatings formed during the PEO (Table 1) does not significantly change the phase structure of TiO_2. Patterns in Fig. 4a suggest that during the PEO anatase is the dominant phase of TiO_2. Careful inspection of XRD patterns reveals that anatase phase TiO_2:Eu^{3+} coatings are formed during the first minute of PEO, while after about 3 min from the onset of PEO anatase phase starts to transform into rutile phase. The main observed peaks are at 2θ angle of 25.4° and 27.5°, which are assigned to anatase (101) and rutile (110) crystalline phases, respectively. The intensity of diffraction peaks of anatase and rutile phases increase with the increasing time of PEO. This suggests that the crystallization increases with PEO time. The content of anatase and rutile phases was calculated from the integrated intensities of the anatase (101) and rutile (110) peaks [40], according to equation (2) and is presented in Table 2:

$$W_R = \frac{I_R}{0.884 I_A + I_R}, \tag{2}$$

where W_R represents the weight fraction of rutile phase, I_A represents the integrated intensity of the anatase (101) peak, and I_R represents the integrated intensity of the rutile (110) peak.

The crystallite size of anatase and rutile phases in the coatings was calculated using the Scherrer's equation of the strongest diffraction reflections of the anatase (101) and rutile (110) planes:

$$D = \frac{K\lambda}{\beta \cos\theta}, \quad (3)$$

where D is the crystallite size in nm, K = 0.94, λ is the wavelength of the incident X-rays in nm, θ is the Bragg angle, and β is full width at half maximum in radians. Table 2 shows that the crystallite size of the anatase and rutile phases of formed coatings increases with PEO time.

For further investigation of chemical nature and composition of obtained coatings and valence state of Eu in doped TiO_2 samples we employed XPS measurements. Typical XPS spectra are shown in Fig. 5a. It can be seen that the spectra show peaks originating from Ti 2p, O 1s P 2s, P 2p, C 1s and Eu 3d. Fig. 5b shows the high-resolution Eu 3d spectra of Eu doped TiO_2 coatings formed after various PEO times. The Eu 3d levels are spin–orbit split into two ($3d_{5/2}$ and $3d_{3/2}$) peaks. In each spectrum, the Eu $3d_{5/2}$ peak is located at 1134.7 eV, indicating Eu^{3+} state [41]. The Ti 2p XPS spectrum obtained for pure TiO_2 coating shows that spin-orbit components ($2p_{3/2}$ and $2p_{1/2}$) are positioned at about 459.0 eV and 464.9 eV, respectively, which can be assigned to Ti^{4+} ions in TiO_2. On the other hand, for all TiO_2:Eu^{3+} coatings XPS peaks associated with spin-orbit components are shifted towards higher binding energies by 0.2 eV (Fig. 5c). This shift in binding energy represents intermediate oxidation state of Ti and indicates that Eu^{3+} is incorporated into TiO_2 lattice.

3.2. Photoluminescence (PL) of TiO_2:Eu^{3+} coatings

PL emission spectra of TiO_2:Eu^{3+}coatings formed after various PEO times excited at 270 nm are shown in Fig. 6a. PL spectra consist of sharp emission bands located in the orange-red spectral region between 560 nm and 720 nm, corresponding to the f–f transition

of Eu^{3+} from excited level $^5D_0$ to lower levels ^7F_J (J = 0, 1, 2, 3, and 4) [42]. The bands are centered at about 578 nm, 591 nm, 596 nm, 613 nm, 653 nm, and 701 nm, and are assigned to the $^5D_0 \rightarrow {}^7F_0$, $^5D_0 \rightarrow {}^7F_1$, $^5D_0 \rightarrow {}^7F_2$, $^5D_0 \rightarrow {}^7F_3$, $^5D_0 \rightarrow {}^7F_4$ transitions, respectively.

Fig. 6b shows the excitation PL spectra of TiO_2:Eu^{3+}coatings formed after various PEO times, monitored at the most intense peak in emission PL spectra, i.e. at 613 nm. The wide PL band extending from 250 nm to 350 nm, with a maximum at about 275 nm, is associated with charge transfer state of Eu^{3+}, which originates from electronic transition between the completely filled 2p orbital of O^{2-} ions ($2p^6$) and empty 4f orbital of Eu^{3+} ions ($4f^6$) [43]. The string of sharp peaks in the range from 350 nm to 550 nm corresponds to direct excitation of the Eu^{3+} ground state $^7F_0$ into higher levels of the 4f-manifold [44]. The most intense excitation bands are assigned to f-f transition $^7F_0 \rightarrow {}^5D_4$ at 360 nm, $^7F_0 \rightarrow {}^5L_7$ at 381 nm, $^7F_0 \rightarrow {}^5L_6$ at 393 nm, $^7F_0 \rightarrow {}^5D_3$ at 413 nm, $^7F_0 \rightarrow {}^5D_2$ at 463 nm, and $^7F_0 \rightarrow {}^5D_1$ at 531 nm.

The total PL intensity of TiO_2:Eu^{3+}coatings is a sum of PL originating from TiO_2 and Eu^{3+} ions incorporated into the coatings during the PEO. In order to investigate PL emission and excitation spectra of pure TiO_2 coatings, we formed such coatings in supporting electrolyte without addition of Eu_2O_3 powder under the same experimental conditions as in Figs. 6a and 6b. PL emission and excitation spectra of pure TiO_2 coating formed in supporting electrolyte for 10 min are shown in Figs. 6c and d. It is obvious that PL of pure TiO_2 coating is very low compared to its counterpart formed in supporting electrolyte with Eu_2O_3 powder, indicating that the main contribution in PL for TiO_2:Eu^{3+} coatings comes from Eu^{3+}. It is clearly visible that the intensity of peaks in excitation and emission PL spectra change with the concentration of Eu^{3+}, i.e. time of PEO, but the peaks position remains practically unchanged.

Fig. 7 shows the energy level diagram and proposed mechanism of charge transfer pathways involved in the PL of Eu^{3+} doped TiO_2 coatings formed by PEO. Excitation may

take place in two processes, either by transferring electrons to the charge transfer band (CTB) or by electron jumping to the higher levels of Eu^{3+}. After the excitation, excited electrons (due to charge transfer) are transferred to the lowest excited level of Eu^{3+} i.e. $^5D_0$ by non-radiative transition. Only upon non-radiative transfer electrons can make transitions to the lower levels ^7F_J (J = 0, 1, 2, 3, and 4) of Eu^{3+}.

PL emission spectra of TiO_2:Eu^{3+}coatings, in the range from 560 nm to 720 nm, excited at the wavelengths of the most intense peaks in PL excitation spectra ($^7F_0 \rightarrow ^5L_6$ transition at 393 nm and $^7F_0 \rightarrow ^5D_2$ transition at 463 nm) are shown in Fig. 8. The strongest red PL peak at 613 nm corresponds to the electric dipole transition $^5D_0 \rightarrow ^7F_2$ ($\Delta J = \pm 2$). The electric dipole transition $^5D_0 \rightarrow ^7F_2$ is a hypersensitive transition (with respect to the local environment around the Eu^{3+} ion), which is allowed only under the condition that Eu^{3+} ion occupies a site without an inversion center [30]. On the other hand, $^5D_0 \rightarrow ^7F_1$ transitions at 591 nm and 596 nm are principally magnetic allowed dipole transitions ($\Delta J = \pm 1$) which are insensitive to site symmetry [45]. The emission intensity ratio *R* between $^5D_0 \rightarrow ^7F_2$ and $^5D_0 \rightarrow ^7F_1$ transitions (also called the asymmetric ratio) can be used as an effective spectroscopic technique to measure the degree of distortion from inversion symmetry of the local environment surrounding the Eu^{3+} ions in the host matrix. The asymmetric ratio between $^5D_0 \rightarrow ^7F_2$ at 613 nm and $^5D_0 \rightarrow ^7F_1$ at 591 nm for two excitation wavelengths at 393 nm and 463 nm is shown in Fig. 4c. The asymmetric ratio increases slightly with increasing Eu^{3+} concentration, i.e. time of PEO, indicating that the symmetry of Eu^{3+} ions does not change much with its concentration [46]. High value of the asymmetric ratio of TiO_2:Eu^{3+} coating formed by PEO indicates highly asymmetric environment around Eu^{3+} ions. The site symmetry of Ti^{4+} ions in anatase lattice are D_{2d}. According to the branching rules of the 32 point groups, because of a large mismatch in ionic radii and the charge imbalance between Ti^{4+} (68 pm) and Eu^{3+} (95 pm), the substitution of the Ti^{4+} with Eu^{3+} ions creates oxygen

vacancies and causes the lattice distortion, thus changing the site symmetry of the Eu^{3+} ions sites from the exact D_{2d} symmetry to lower site symmetry [47]. Weak PL emission bands at 653 nm and 701 nm are due to forbidden $^5D_0 \rightarrow {}^7F_3$ and electric dipole allowed $^5D_0 \rightarrow {}^7F_4$ transitions, respectively. It is worth mentioning that we observed the totally forbidden $^5D_0 \rightarrow {}^7F_0$ transition at 578 nm, which becomes allowed only in the case where the site symmetry of the metal ions is C_{nv} or lower [48,49].

3.3. Photocatalytic activity (PA) of TiO_2:Eu^{3+} coatings

Before the PA characterization we investigated optical absorption of TiO_2:Eu^{3+}coatings formed after various PEO times (Fig. 9). UV–Vis DRS spectra of TiO_2:Eu^{3+}coatings show that the increasing amount of incorporated Eu^{3+} gradually shifted absorption edge of pure TiO_2 from the UV to the visible range. Observed red shift can be attributed to the charge-transfer transition between f electrons of Eu^{3+} ions and the conduction or valence band of TiO_2 [50].

The Kubelka-Munk function $F(R_\infty)$ for infinitely thick samples was used to convert reflectance measurements (R_{sample}) into equivalent absorption spectra:

$$F(R_\infty) = \frac{(1-R_\infty)^2}{2R_\infty} = \frac{\alpha}{S}, \quad (4)$$

where α and S denote to the absorption coefficient and the scattering coefficient, respectively. This is achieved by using the reflectance of $BaSO_4$ as a reference (R_{BaSO4}):

$$R_\infty = \frac{R_{sample}}{R_{BaSO_4}}, \quad (5)$$

The optical absorption edge energy is defined as the minimum photon energy required to excite an electron from the highest occupied molecular orbital (HOMO, at the top of the valence band) to the lowest unoccupied molecular orbital (LUMO, at the bottom of the

conduction band). The energy dependence of the absorption coefficient α for semiconductors in the region near the absorption edge is given by the equation:

$$\alpha \propto \frac{(h\nu - E_g)^{\eta}}{h\nu}, \quad (6)$$

where ν is the frequency of the incident photon, h is the Planck constant, and E_g is the optical absorption edge energy. The exponent η depends on the type of optical transition caused by photon absorption. With an appropriate choice of η, a plot of $[F(R_\infty)h\nu]^{1/\eta}$ vs. $h\nu$ (Tauc plot) is linear near the edge and can be used to determine the absorption edge energy, i.e. the band gap. For TiO_2 material, the value of η is 2 [51], and we used this value to plot $[F(R_\infty)h\nu]^{1/2}$ vs. $h\nu$ for TiO_2:Eu^{3+} coatings formed in various stages of PEO, as shown in Fig. 10. The band gap shifts to lower energy with increasing PEO time, i.e. with increasing amount of Eu^{3+}. The band gaps of obtained TiO_2:Eu^{3+} coatings as well as of pure TiO_2 coatings are listed in Table 3. Clearly, the main contribution in the reduction of band gap in TiO_2:Eu^{3+} coatings is due to the incorporation of Eu in TiO_2 coatings during the PEO.

Photoactivity of pure TiO_2 and TiO_2:Eu^{3+}coatings formed after various PEO times are shown in Fig. 11. C_0 is the initial concentration of MO and C is the concentration after time t. Fig. 11a clearly implies that PA of TiO_2:Eu^{3+}coatings is much higher than of pure TiO_2. Knowing that pure Eu_2O_3 does not have photocatalytic oxidation properties, such variation in PA is due to interaction between Eu^{3+} ions and TiO_2. In order to explain the influence of PEO time on PA of formed coatings we constructed a plot at Fig. 11b which presents PA after 10 h of irradiation for pure TiO_2 and TiO_2:Eu^{3+} coatings (formed for various PEO times). It is evident that there is a substantially different PA behavior of formed coatings: PA of pure TiO_2 coatings rises with PEO time, while PA of TiO_2:Eu^{3+} coatings surprisingly drops with PEO time. It is challenging to find out a reasonable explanation for such behavior of TiO_2:Eu^{3+} coatings having in mind that thicknesses, surface area, and phase composition of TiO_2, i.e.

ratio between anatase and rutile (Table 2), are supposed to be approximately equivalent for both coatings. It is well known that catalyst's PA is mainly dependent upon band gap value, surface texture, electron-hole generation capacity, separation efficiency of photogenerated electron/hole pairs, and transfer of electrons from photacatalyst to the organic pollutant through the oxygen vacancy defects on the surface of photocatalyst [52]. Incorporation of Eu^{3+} ions into TiO_2 coatings during the PEO could create oxygen vacancy charge trapping centers, thus decreasing the electron/hole recombination rate. For these reasons PA of TiO_2:Eu^{3+}coatings might increases with respect to pure TiO_2 coatings. The rise of the Eu^{3+} concentration in coatings with PEO time expands the spectral region that can be used for visible light photocatalysis (Figs. 9 and 10). Fig. 11b clearly shows that after 10 h of irradiation PA of TiO_2:Eu^{3+} coatings obtained after 1 min of PEO is almost 70 % higher than PA of corresponding pure TiO_2 coatings, while it is only about 10 % higher for samples obtained after 10 min of PEO time.

Since TiO_2:Eu^{3+} coatings formed after 1 min of PEO unambiguously exhibit the best photocatalytic performance, one can assume that specific active centers are created within the coating and/or these coatings exhibit superior morphology with respect to PEO coatings processed for longer times. SEM micrographs (Fig. 2b) reveal that PEO coatings obtained for the shortest processing time feature exceptionally developed outer surface which consists of small grains (2-3 μm in diameter). With prolonged PEO time this outer surface flattens leaving pancake-like surface structure with holes originating from discharge channels. Such morphology change, caused primarily by increased temperature during microdischarging, possibly affects the overall surface area of the coating, either by reducing the number of active sites or simply by blocking the transport of reactants (light as immaterial reactant and/or dye).

Concurrently, TiO_2:Eu^{3+} catalyst formed after 1 min of PEO contains only anatase phase of TiO_2 producing high degree of structure organization around incorporated Eu^{3+} ions. Transformation of anatase to rutile by prolonged PEO process time probably causes the distortion of Eu^{3+} surrounding lattice as presented on Fig. 8c. The rise of asymmetric ratio between $^5D_0 \rightarrow {}^7F_2$ and $^5D_0 \rightarrow {}^7F_1$, as the measure of distortion degree, also increases with PEO time. As a consequence, it is clear that Eu^{3+} ions in this case could serve as electron/hole recombination centers, pointing that Eu^{3+} surrounding is more significant than Eu^{3+} concentration when photocatalytic application of TiO_2:Eu^{3+} coatings is concerned.

An important parameter for the applicability of the photocatalyst is its stability, which determines the catalyst life and operation cost. The PA after 12 h of irradiation after five consecutive runs using TiO_2:Eu^{3+} coating formed for 1 min is presented in Fig. 12. After each run, the sample was rinsed in water, dried, and used again in the next catalytic run. The results show that PA of the coating remains almost unchanged after several consecutive runs, proving that there is neither significant attrition of photocatalyst from the support nor catalyst poisoning.

In order to investigate the influence of Eu_2O_3 concentration in electrolyte on photocatalytic properties of obtained coatings another set of measurements was conducted in supporting electrolyte (10 g/L $Na_3PO_4 \cdot 12H_2O$) with various Eu_2O_3 concentrations (Fig. 13). Obviously, there is no difference in PA for Eu_2O_3 concentrations of 2g/L and 3 g/L, but concentration of 0.5 g/L causes significant drop in PA. The main reason for this behavior lies in the fact that the concentration of Eu_2O_3 in the electrolyte has low influence on the morphology and chemical composition of the formed coatings under the same experimental conditions.

4. Conclusions

In summary, TiO_2:Eu^{3+} coatings were prepared by plasma electrolytic oxidation (PEO) of titanium in electrolyte containing Eu_2O_3 powder. Structural, photoluminescent and photocatalytic properties of obtained oxide coatings were investigated. The main elemental components of the PEO coatings are Ti, O, P, Eu. Elemental mapping analyses showed that coatings' elements are distributed evenly, with some Eu agglomerations being observed after prolonged PEO times. The PEO coatings are crystallized and composed of anatase and rutile TiO_2 phases, with anatase being the dominant phase. XPS analyses confirmed that Eu^{3+} ions are incorporated into coatings and it pointed out that Ti 2p spin-orbit components in composite coatings are shifted towards higher binding energy with respect to pure TiO_2 coatings. Optical absorption spectra of TiO_2:Eu^{3+}coatings exhibit evident red shift with respect to pure TiO_2 coatings.

PL emission spectra of TiO_2:Eu^{3+} coatings are characterized by sharp emission bands in orange-red region ascribed to $^5D_0 \rightarrow {}^7F_J$ transitions of Eu^{3+} ions. Excitation PL spectra of TiO_2:Eu^{3+} coatings are characterized by a broad band extending from 250 nm to 350 nm, with a maximum at about 275 nm. This broad band is associated with the electron transfer transition from 2p orbital of O^{2-} ions to 4f orbital of Eu^{3+} ions, while the series of sharp peaks in the range from 350 nm to 550 nm corresponds to direct excitation of the Eu^{3+} ground state $^7F_0$ into higher levels of the 4f-manifold. Electrical dipole transition $^5D_0 \rightarrow {}^7F_2$ is much more intense than the magnetic dipole transition $^5D_0 \rightarrow {}^7F_1$, suggesting the presence of the Eu^{3+} ions in highly asymmetric environment.

TiO_2:Eu^{3+} coatings show much higher photocatalytic activity (PA) than pure TiO_2 coatings. The time of PEO, i.e. the amount of Eu^{3+} incorporated into coatings, is an important factor affecting PA and the TiO_2:Eu^{3+} coating formed after 1 min of PEO time exhibits the highest photoactivity.

Acknowledgements

This work is supported by the Ministry of Education, Science, and Technological Development of the Republic of Serbia under projects No. 171035, 172022, and 172026.

References:

[1] B. Hu, B. Liu, Dye-sensitized solar cells fabricated by the TiO_2 nanostructural materials synthesized by electrospray and hydrothermal post-treatment, Appl. Surf. Sci. 358 (2015) 412–417.

[2] H.T. Chen, H.Y. Shu, C.J. Chung, J.L. He, Assessment of bone morphogenic protein and hydroxyapatite–titanium dioxide composites for bone implant materials, Surf. Coat. Technol. 276 (2015) 168–174.

[3] W. Chen, A. Zhou, Xin Yang, Yan Liu, Synthesis, structure and luminescence properties of TiO_2:Eu^{3+} for white light-emitting diode, J. Alloys Compd. 581 (2013) 330–334.

[4] T. Suwannaruang, K.K.P. Rivera, A. Neramittagapong, K.Wantala, Effects of hydrothermal temperature and time on uncalcined TiO_2 synthesis for reactive red 120 photocatalytic degradation, Surf. Coat. Technol. 271 (2015) 192–200.

[5] J. Wen, X. Li, W. Liu, Y. Fang, J. Xie, Y. Xu, Photocatalysis fundamentals and surface modification of TiO_2 nanomaterials, Chin. J. Catal. 36 (2015) 2049–2070.

[6] A Conde-Gallardo, M García-Rocha, R Palomino-Merino, M.P Velásquez-Quesada, I Hernández-Calderón, Photoluminescence properties of Tb^{3+} and Eu^{3+} ions hosted in TiO_2 matrix, Appl. Surf. Sci. 212–213 (2003) 583–588.

[7] J. Domaradzki, E.L. Prociow, D. Kaczmarek, A. Borkowska, T. Berlicki, K. Prociow, Structural and optical properties of terbium in TiO_2 matrix, Opt. Mater. 31 (2009) 1349–1352.

[8] M. Vranješ, J. Kuljanin-Jakovljević, T. Radetić, M. Stoiljković, M. Mitrić, Z.V. Šaponjić, J. Nedeljković, Structure and luminescence properties of Eu^{3+} doped TiO_2 nanocrystals and

prolate nanospheroids synthesized by the hydrothermal processing, Ceram. Int. 38 (2012) 5629–5636.

[9] M. Vranješ, J. Kuljanin-Jakovljević, S.P. Ahrenkiel, I. Zeković, M. Mitrić, Z. Šaponjić, J.M. Nedeljković, Sm^{3+} doped TiO_2 nanoparticles synthesized from nanotubular precursors—luminescent and structural properties, J. Lumin. 143 (2013) 453–458.

[10] Y. Sheng, L. Zhang, H. Li, J. Xue, K. Zheng, N. Guo, Q. Huo, H. Zou, Photoluminescence of TiO_2 films co-doped with Tb^{3+}/ $Gd^{3+}$and energy transfer from TiO_2/Gd^{3+} to Tb^{3+} ions, Thin Solid Films 519 (2011) 7966–7970.

[11] L. Dolgov, V. Reedo, V. Kiisk, S. Pikker, I. Sildos, J. Kikas, Structure and fluorescent properties of TiO_2:Sm^{3+}–Ag composite, Opt. Mater. 32 (2010) 1540–1544.

[12] V. Kiisk, V. Reedo, M. Karbowiak, M.G. Brik, I. Sildos, Spectroscopic and crystal field study of Sm^{3+} in different phases of TiO_2, J. Phys. D: Appl. Phys. 42 (2009) 125107 (6pp).

[13] J. Reszczyńska, T. Grzyb, J.W. Sobczak, W. Lisowski, M. Gazda, B. Ohtani, A. Zaleska, Lanthanide co-doped TiO_2: The effect of metal type and amount on surface properties and photocatalytic activity, Appl. Surf. Sci. 307 (2014) 333–345.

[14] V. Stengl, S. Bakardjieva, N. Murafa, Preparation and photocatalytic activity of rare earth doped TiO_2 nanoparticles, Mater. Chem. Phys. 114 (2009) 217–226.

[15] D.M. Tobaldi, R.C. Pulla, A.S. Skapin, M.P. Seabra, J.A. Labrinch, Visible light activated photocatalytic behaviour of rare earth modified commercial TiO_2, Mater. Res. Bull. 50 (2014) 183–190.

[16] E. Setiawati, K. Kawano, Stabilization of anatase phase in the rare earth; Eu and Sm ion doped nanoparticle TiO_2, J. Alloys Compd. 451 (2008) 293–296.

[17] L.G. Devi, S.G. Kumar, Exploring the critical dependence of adsorption of various dyes on the degradation rate using Ln^{3+}-TiO2 surface under UV/solar light, Appl. Surf. Sci. 261 (2012) 137–146.

[18] A.S. Weber, A.M. Grady, R.T. Koodali, Lanthanide modified semiconductor photocatalysts, Catal. Sci. Technol. 2 (2012) 683–693.

[19] Y. Yu, G. Chen, Y. Zhou, Z. Han, Recent advances in rare-earth elements modification of inorganic semiconductor based photocatalysts for efficient solar energy conversion: A review, J. Rare Earths 33 (2015) 453–462.

[20] R. Wang, F. Wang, S. An, J. Song, Y. Zhang, Y/Eu co-doped TiO_2: synthesis and photocatalytic activities under UV-light, J. Rare Earths 33 (2015) 154–159.

[21] J. Puskelova, R. Michal, M. Caplovicova, M. Antoniadou, L. Caplovic, G. Plesch, P. Lianos, Hydrogen production by photocatalytic ethanol reforming using Eu-and S-doped anatase, Appl. Surf. Sci. 305 (2014) 665–669.

[22] E. Le Boulbar, E. Millon, C. Boulmer-Leborgne, C. Cachoncinlle, B. Hakim, E. Ntsoenzok, Optical properties of rare earth-doped TiO_2 anatase and rutile thin films grown by pulsed-laser deposition, Thin Solid Films 553 (2014) 13–16.

[23] E. Zaleta-Alejandre, M. Zapata-Torres, M. Garcıa-Hipolito, M. Aguilar-Frutis, G. Alarcon-Flores, J. Guzman-Mendoza, C. Falcony, Structural and luminescent properties of europium doped TiO_2 thick films synthesized by the ultrasonic spray pyrolysis technique, J. Phys. D: Appl. Phys. 42 (2009) 095102 (7pp).

[24] M. Borlaf, R. Moreno, A.L. Ortiz, M.T. Colomer, Synthesis and photocatalytic activity of Eu^{3+}-doped nanoparticulate TiO_2 sols and thermal stability of the resulting xerogels, Mater. Chem. Phys. 144 (2014) 8–16.

[25] X. Qi, Y Song, Y. Sheng, H. Zhang, H. Zhao, Z. Shi, H Zou, Controllable synthesis and luminescence properties of TiO_2:Eu^{3+} nanorods, nanoparticles and submicrospheres by hydrothermal method, Opt. Mater. 38 (2014) 193–197.

[26] M. Ikeda, J.G. Li, N. Kobayashi, Y. Moriyoshi, H. Hamanaka, T. Ishigaki, Phase formation and luminescence properties in Eu^{3+}-doped TiO_2 nanoparticles prepared by thermal plasma pyrolysis of aqueous solutions, Thin Solid Films 516 (2008) 6640–6644.

[27] A.L. Yerokhin, X. Nie, A. Leyland, A. Matthews, S.J. Dowey, Plasma electrolysis for surface engineering, Surf. Coat. Technol. 122 (1999) 73–93.

[28] S. Stojadinović, N. Tadić, N. Radić, B. Stojadinović, B. Grbić, R. Vasilić, Synthesis and characterization of Al2O3/ZnO coatings formed by plasma electrolytic oxidation, Surf. Coat. Technol. 276 (2015) 573–579.

[29] S. Stojadinović, R. Vasilić, M. Perić, Investigation of plasma electrolytic oxidation on valve metals by means of molecular spectroscopy – a review, RSC Adv. 4 (2014) 25759–25789.

[30] S. Stojadinović, N. Radić, R. Vasilić, M. Petković, P. Stefanov, Lj. Zeković, B. Grbić, Photocatalytic properties of TiO_2/WO_3 coatings formed by plasma electrolytic oxidation of titanium in 12-tungstosilicic acid, Appl. Catal., B 126 (2012) 334–341.

[31] M.R. Bayati, A.Z. Moshfegh, F. Golestani-Fard, On the photocatalytic activity of the sulfur doped titania nano-porous films derived via micro-arc oxidation, Appl. Catal., A 389 (2010) 60–67.

[32] H.J. Oh, C.S. Chi, Eu–N-doped TiO_2 photocatalyst synthesized by micro-arc oxidation, Mater. Lett. 86 (2012) 31–33.

[33] D. Chen, Q. Zhu, Z. Lv, X. Deng, F. Zhou, Y. Deng, Microstructural and photocatatlytic properties of Eu-doped mesporous titanium dioxide nanopaticles by sol–gel method, Mater. Res. Bull. 47 (2012) 3129–3134.

[34] L. Diamandescu, F. Vasiliu, D. Tarabasanu-Mihaila, M. Feder, A.M. Vlaicu, C.M. Teodorescu, D. Macovei, I. Enculescu, V. Parvulescu, E. Vasile, Structural and photocatalytic

properties of iron- and europium-doped TiO_2 nanoparticles obtained under hydrothermal conditions, Mater. Chem. Phys. 112 (2008) 146–153.

[35] Z.M. El-Bahy, A.A. Ismail, R.M. Mohamed, Enhancement of titania by doping rare earth for photodegradation of organic dye (Direct Blue), J. Hazard. Mater. 166 (2009) 138–143.

[36] J.L. Delplancke, R. Winand, Galvanostatic anodization of titanium—II. Reactions efficiencies and electrochemical behaviour model, Electrochim. Acta 33 (1988) 1551–1559.

[37] A. L. Yerokhin, V. V. Lyubimov and R. V. Ashitkov, Phase formation in ceramic coatings during plasma electrolytic oxidation of aluminium alloys, Ceram. Int. 24 (1998) 1–6.

[38] S. Stojadinović, R. Vasilić, M. Petković, B. Kasalica, I. Belča, A. Žekić, Lj. Zeković, Characterization of the plasma electrolytic oxidation of titanium in sodium metasilicate, Appl. Surf. Sci. 265 (2013) 226–233.

[39] X. Lu, C. Blawert, M.L. Zheludkevich, K.U. Kainer, Insights into plasma electrolytic oxidation treatment with particle addition, Corros. Sci. 101 (2015) 201–207.

[40] H. Zhang, J.F. Banfield, Understanding polymorphic phase transformation behavior during growth of nanocrystalline aggregates: insights from TiO_2, J. Phys. Chem. B 104 (2000) 3481–3487.

[41] S. Kumar, R. Prakash, R.J. Choudhary, D.M. Phase, Structural, XPS and magnetic studies of pulsed laser deposited Fe doped Eu_2O_3 thin film, Mater. Res. Bull. 70 (2015) 392–396.

[42] B.K. Moon, I.M. Kwon, H.K. Yang, H.J. Seo, J.H. Jeong, S.S. Yi, J.H. Kim, Spectroscopy of nanocrystalline TiO_2:Eu^{3+} phosphors, Colloids Surf., A 313–314 (2008) 82–86.

[43] Q.G. Zeng, Z.M. Zhang, Z.J. Ding, Y. Wang, Y.Q. Sheng, Strong photoluminescence emission of Eu:TiO_2 nanotubes, Scr. Mater. 57 (2007) 897–900.

[44] H. Li, Y. Sheng, H. Zhao, Y. Song, F. Gao, Q. Huo, H. Zou, Facile synthesis and luminescent properties of TiO_2:Eu^{3+} nanorods and spindle-shaped nanoparticles from titanate nanotubes precursors, Mater. Res. Bull. 47 (2012) 4322–4328.

[45] M. Chang, Y. Song, H. Zhang, Y. Sheng, K. Zheng, X. Zhou, H. Zou, Hydrothermal assisted sol–gel synthesis and multisite luminescent properties of anatase TiO_2:Eu^{3+} nanorods, RSC Adv. 5 (2015) 59314–59319.

[46] J.G. Li, X. Wang, K. Watanabe, T. Ishigaki, Phase structure and luminescence properties of Eu^{3+}-doped TiO_2 nanocrystals synthesized by Ar/O_2 radio frequency thermal plasma oxidation of liquid precursor mists, J. Phys. Chem. B 110 (2006) 1121–1127.

[47] M. Yan, H. Zou, H. Zhao, Y. Song, K. Zheng, Y. Sheng, G. Wang, Q. Huo, Fabrication and photoluminescence properties of TiO_2:Eu^{3+} microspheres with tunable structure from solid to core–shell, CrystEngComm 16 (2014) 9216–9223.

[48] M. Mohapatra, Y.P. Naik, V. Natarajan, T.K. Seshagiri, S.V. Godbole, Photoluminescence properties of Eu^{3+} in lithium titanate, Physica B 406 (2011) 1977–1982.

[49] W. Luo, R. Li, G. Liu, M.R. Antonio, X. Chen, Evidence of trivalent europium incorporated in anatase TiO_2 nanocrystals with multiple sites, J. Phys. Chem. C 112 (2008) 10370–10377.

[50] A.W. Xu, Y. Gao, H.Q. Liu, The Preparation, characterization, and their photocatalytic activities of rare-earth-doped TiO_2 nanoparticles, J. Catal. 207 (2002) 151–157.

[51] J.H. Huang, P.Y. Hung, S.F. Hu, R.S. Liu, Improvement efficiency of a dye-sensitized solar cell using Eu^{3+} modified TiO_2 nanoparticles as a secondary layer electrode, J. Mater. Chem. 20 (2010) 6505–6511.

[52] Y. Zheng, C. Chen, Y. Zhan, X. Lin, Q. Zheng, K. Wei, J. Zhu, Photocatalytic activity of Ag/ZnO heterostructure nanocatalyst: correlation between structure and property. J. Phys. Chem. C 112 (2008) 10773–10777.

Figure Captions:

Fig. 1. Experimental setup used for PEO: (1) electrolytic cell; (2) power supply; (3) magnetic stirrer; (4) peristaltic pump; (5) heat exchanging system; (6) temperature-controlled water bath.

Fig. 2. (a) Time variation of voltage and thickness of formed coatings during anodization of titanium in 10 g/L $Na_3PO_4 \cdot 12H_2O$ + 2 g/L Eu_2O_3 at constant current density of 150 mA/cm^2.

(b) SEM micrographs of TiO_2:Eu^{3+} coatings formed at various stages of PEO process: (i) 1 min; (ii) 3 min; (iii) 5 min; (iv) 10 min. (c) Backscattered SEM micrographs of polished

cross-sections of TiO_2:Eu^{3+} coatings formed at various stages of PEO process: (i) 1 min; (ii) 3 min; (iii) 5 min; (iv) 10 min.

Fig. 3. EDS maps of TiO_2:Eu^{3+} coating formed by PEO for 10 min.

Fig. 4. (a) XRD patterns of TiO_2:Eu^{3+} coatings formed at various stages of PEO; (b) XRD pattern of used Eu_2O_3 powder.

Fig. 5. (a) XPS spectra of TiO_2 and TiO_2:Eu^{3+} coatings formed by PEO for 1 min; (b) High – resolution Eu 3d XPS spectra of TiO_2:Eu^{3+} coatings formed at various stages of PEO process; (c) High – resolution Ti 2p XPS spectra of TiO_2 and TiO_2:Eu^{3+} coatings formed by PEO for 1 min.

Fig. 6. Evolution of PL spectra of TiO_2:Eu^{3+} coatings formed by PEO process: (a) emission PL spectra excited at 270 nm; (b) excitation PL spectra monitored at 613 nm. PL spectra of pure TiO_2 coating formed by PEO for 10 min: (c) emission PL spectra excited at 270 nm; (d) excitation PL spectra monitored at 613 nm.

Fig. 7. Schematic representation of energy level diagram and proposed mechanism of charge transfer pathways involved in the PL of Eu^{3+} in TiO_2 coatings formed by PEO.

Fig. 8. Evolution of PL emission spectra of TiO_2:Eu^{3+} coatings formed by PEO process: (a) excited at 393 nm; (b) excited at 463 nm. (c) The asymmetric ratio between $^5D_0 \rightarrow {}^7F_2$ and $^5D_0 \rightarrow {}^7F_1$.

Fig. 9. UV–Vis DRS spectra of pure TiO_2 formed in electrolyte without Eu_2O_3 powder for 1 min and TiO_2:Eu^{3+} coatings formed at various stages of PEO process.

Fig. 10. Tauc plots of pure TiO_2 and TiO_2:Eu^{3+} coatings formed at various stages of PEO process.

Fig. 11. (a) PA of pure TiO_2 and TiO_2:Eu^{3+} coatings formed at various stages of PEO process; (b) The influence of PEO time on PA of pure TiO_2 and TiO_2:Eu^{3+} coatings after 10 h of irradiation.

Fig. 12. PA stability test after 12 h of irradiation of TiO_2:Eu^{3+} coating formed for 1 min of PEO.

Fig. 13. Photocatalytic performance of TiO_2:Eu^{3+} coatings formed for 1 min of PEO in supporting electrolyte (10 g/L $Na_3PO_4 \cdot 12H_2O$) with various Eu_2O_3 concentrations.

Table Captions:

Table 1. EDS analyses of TiO_2:Eu^{3+} coatings formed at various stages of PEO process (Fig. 1a).

Table 2. Weight fraction of anatase phase (W_A), weight fraction of rutile phase (W_R), anatase crystallite size (D_A) and rutile crystallite size (D_R) of TiO_2:Eu^{3+} coatings formed in various stages of PEO.

Table 3. The band gap of TiO_2:Eu^{3+} and TiO_2 coatings formed at various stages of PEO process.

Highlight

- TiO_2:Eu^{3+} coatings are formed by plasma electrolytic oxidation (PEO).
- Photoluminescence is related to transitions of Eu^{3+} from level $^5D_0$ to levels ^7F_J.
- Eu^{3+} ions occupy non-inversion symmetry sites in the coatings.
- PEO time is an important factor affecting photocatalytic activity.

PEO time [min]	Atomic [%]

	O	P	Ti	Eu
1	69.51	4.29	26.16	0.04
3	71.99	4.40	23.46	0.15
5	72.63	4.34	22.83	0.20
10	73.92	4.36	21.37	0.34

PEO time	W_A (%)	W_R (%)	D_A (nm)	D_R (nm)
1 min	100	0	41.7	/
3 min	95.5	4.5	43.3	30.5
5 min	91.1	8.9	46.2	35.6
10 min	87.1	12.9	48.1	44.9

PEO time	Band gap $TiO_2:Eu^{3+}$	Band gap TiO_2
1 min	3.19 eV	3.20 eV
3 min	3.12 eV	3.16 eV
5 min	3.07 eV	3.16 eV
10 min	3.05 eV	3.16 eV

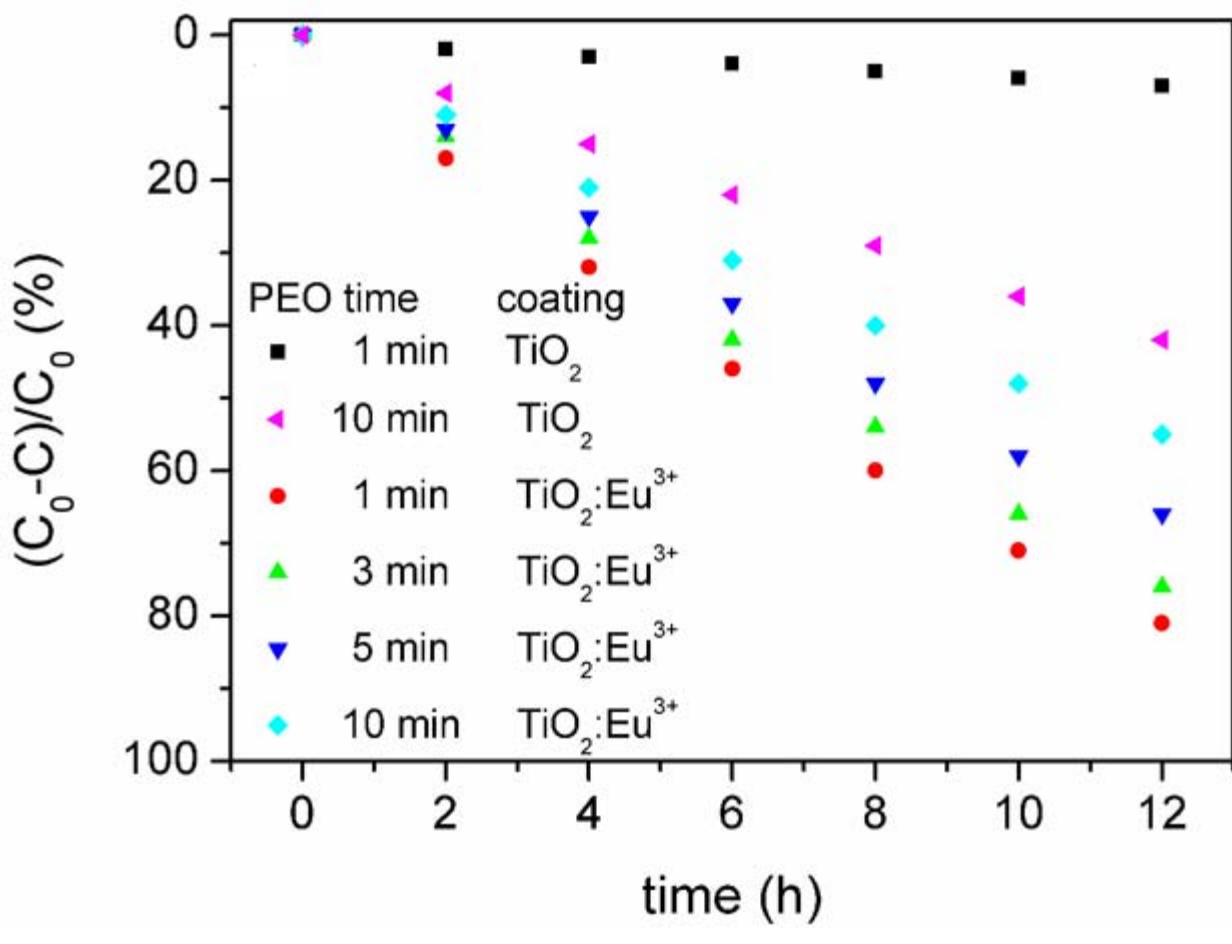
0
20
40
60
80
100
0
2
4
6
8
10
12
time (h)
(C0-C)/C0 (%)
PEO time
coating
1 min
TiO2
10 min
TiO2
1 min
TiO2:Eu3+
3 min
TiO2:Eu3+
5 min
TiO2:Eu3+
10 min
TiO2:Eu3+

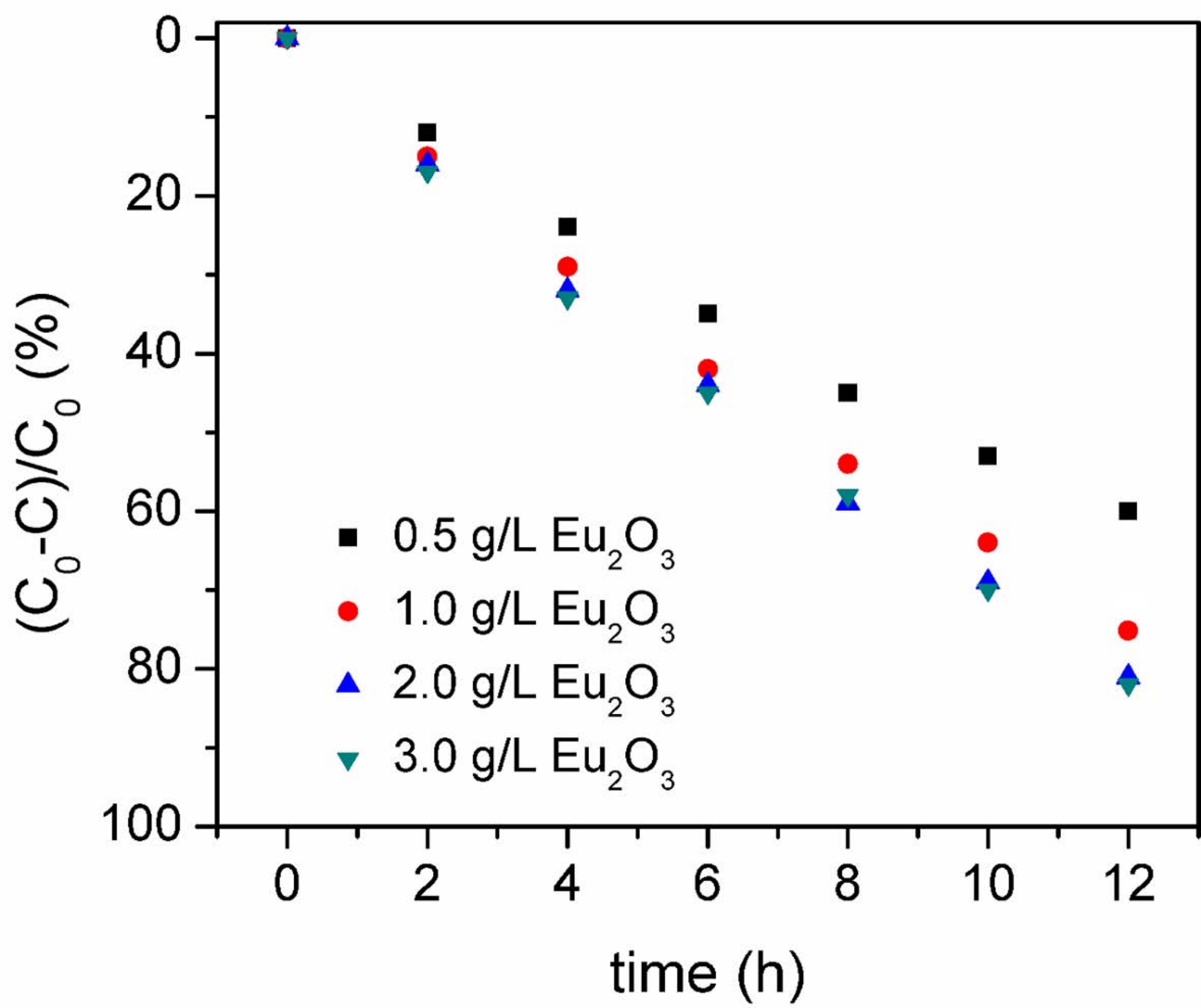
0
20
40
60
80
100
(C0-C)/C0 (%)
0
2
4
6
8
10
12
time (h)
0.5 g/L Eu2O3
1.0 g/L Eu2O3
2.0 g/L Eu2O3
3.0 g/L Eu2O3

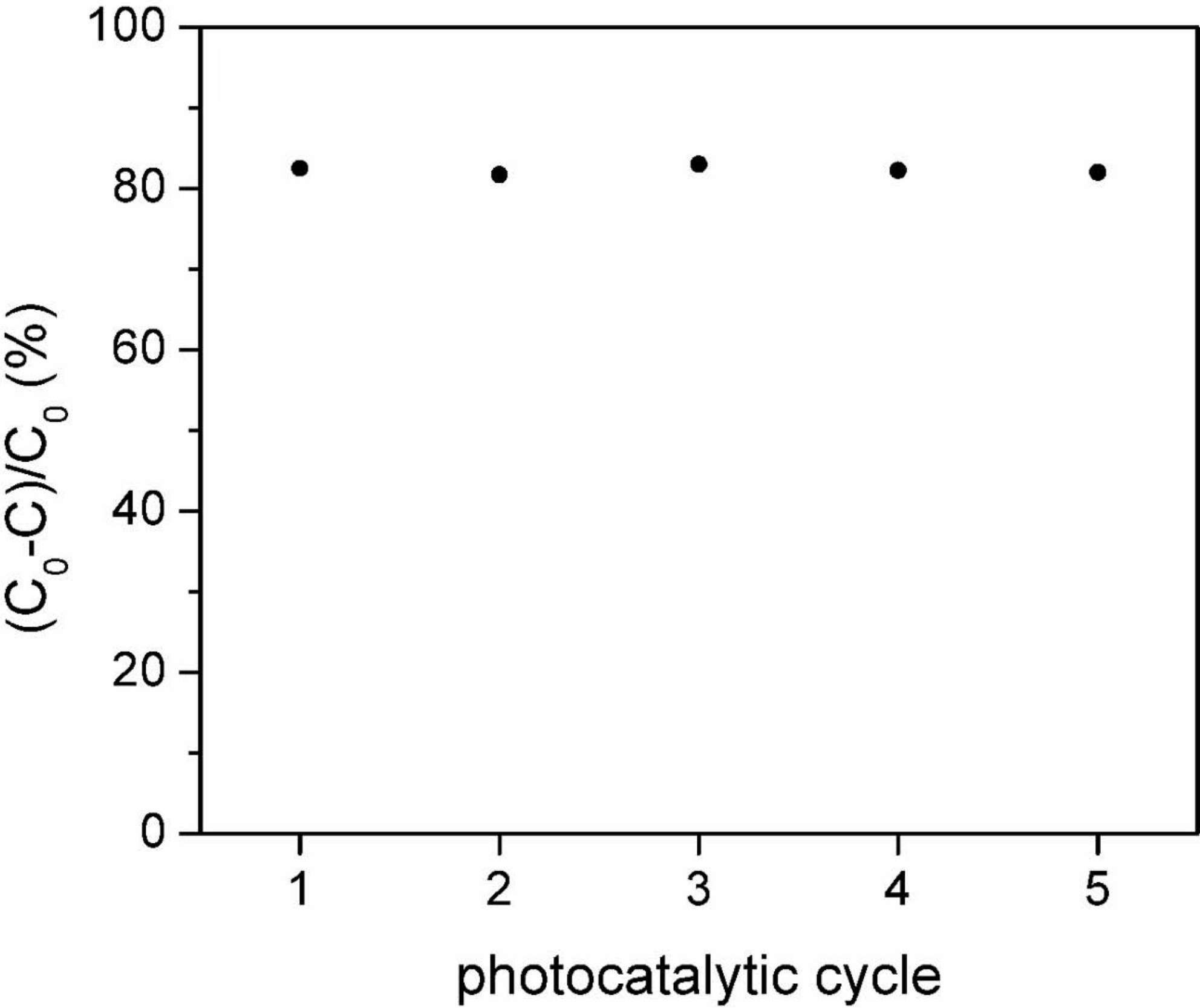
100
80
60
40
20
0
$(C_0-C)/C_0$ (%)
1
2
3
4
5
photocatalytic cycle

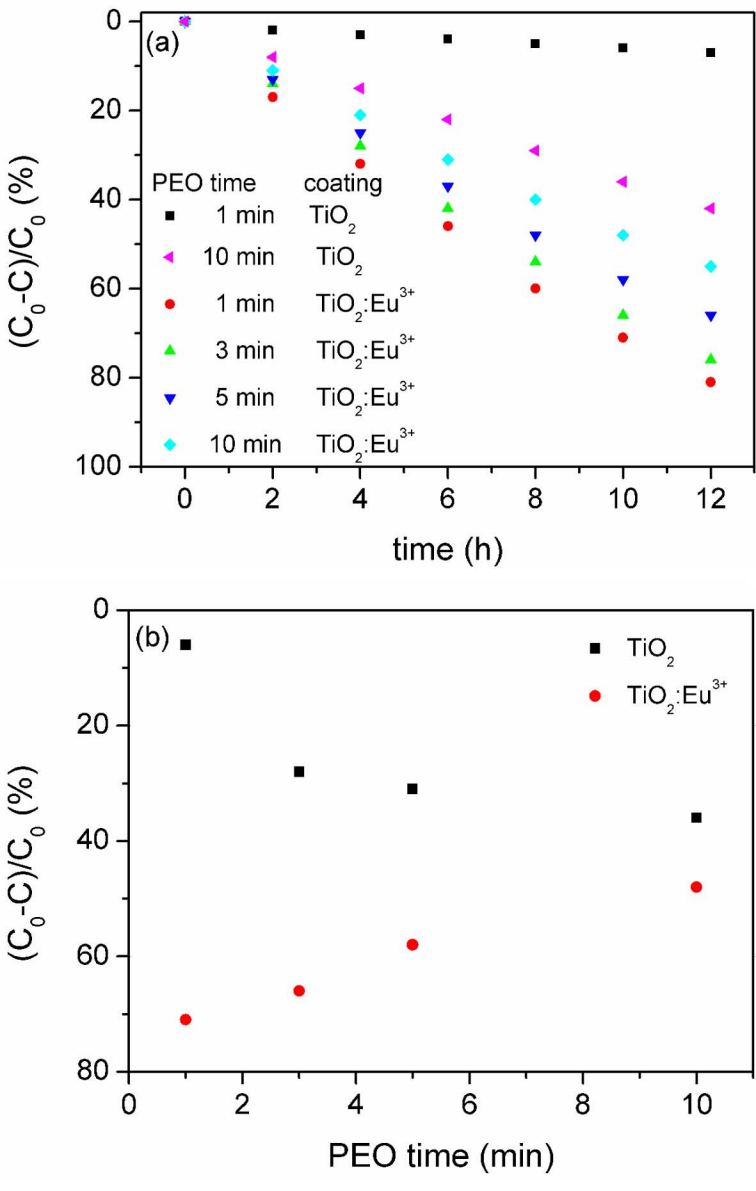
(a)
PEO time
coating
1 min
TiO2
10 min
TiO2
1 min
TiO2:Eu3+
3 min
TiO2:Eu3+
5 min
TiO2:Eu3+
10 min
TiO2:Eu3+
(C0-C)/C0 (%)
time (h)
(b)
TiO2
TiO2:Eu3+
(C0-C)/C0 (%)
PEO time (min)

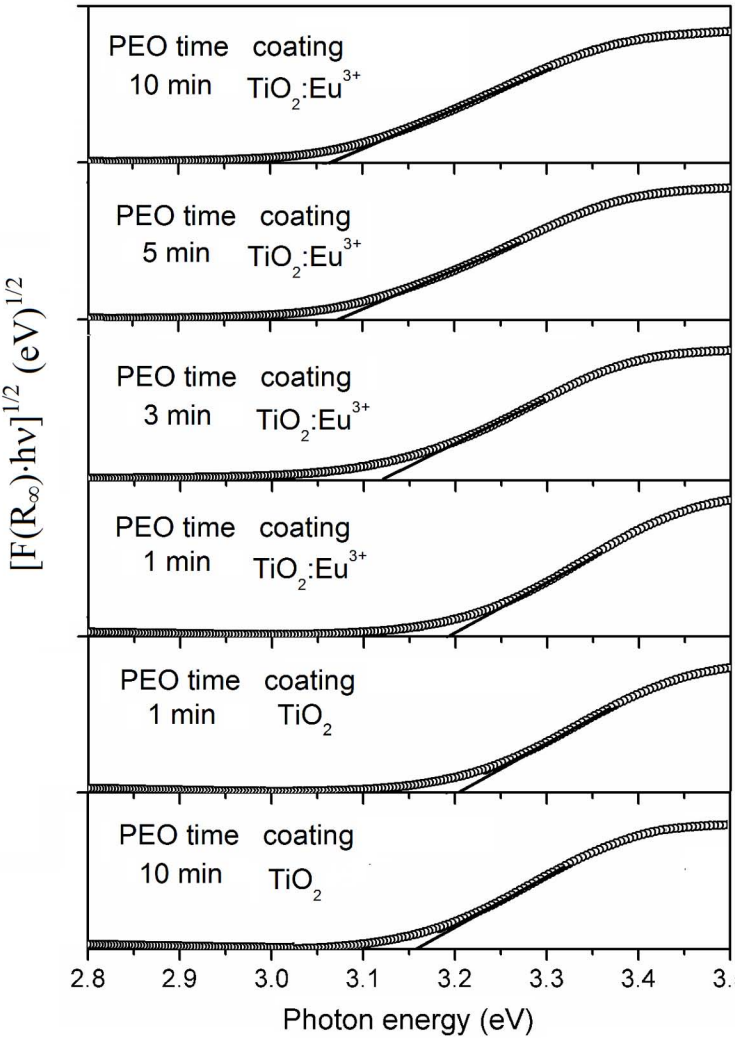
PEO time coating
10 min TiO2:Eu3+
PEO time coating
5 min TiO2:Eu3+
PEO time coating
3 min TiO2:Eu3+
PEO time coating
1 min TiO2:Eu3+
PEO time coating
1 min TiO2
PEO time coating
10 min TiO2
[F(R∞)·hν]1/2 (eV)1/2
2.8
2.9
3.0
3.1
3.2
3.3
3.4
3.5
Photon energy (eV)

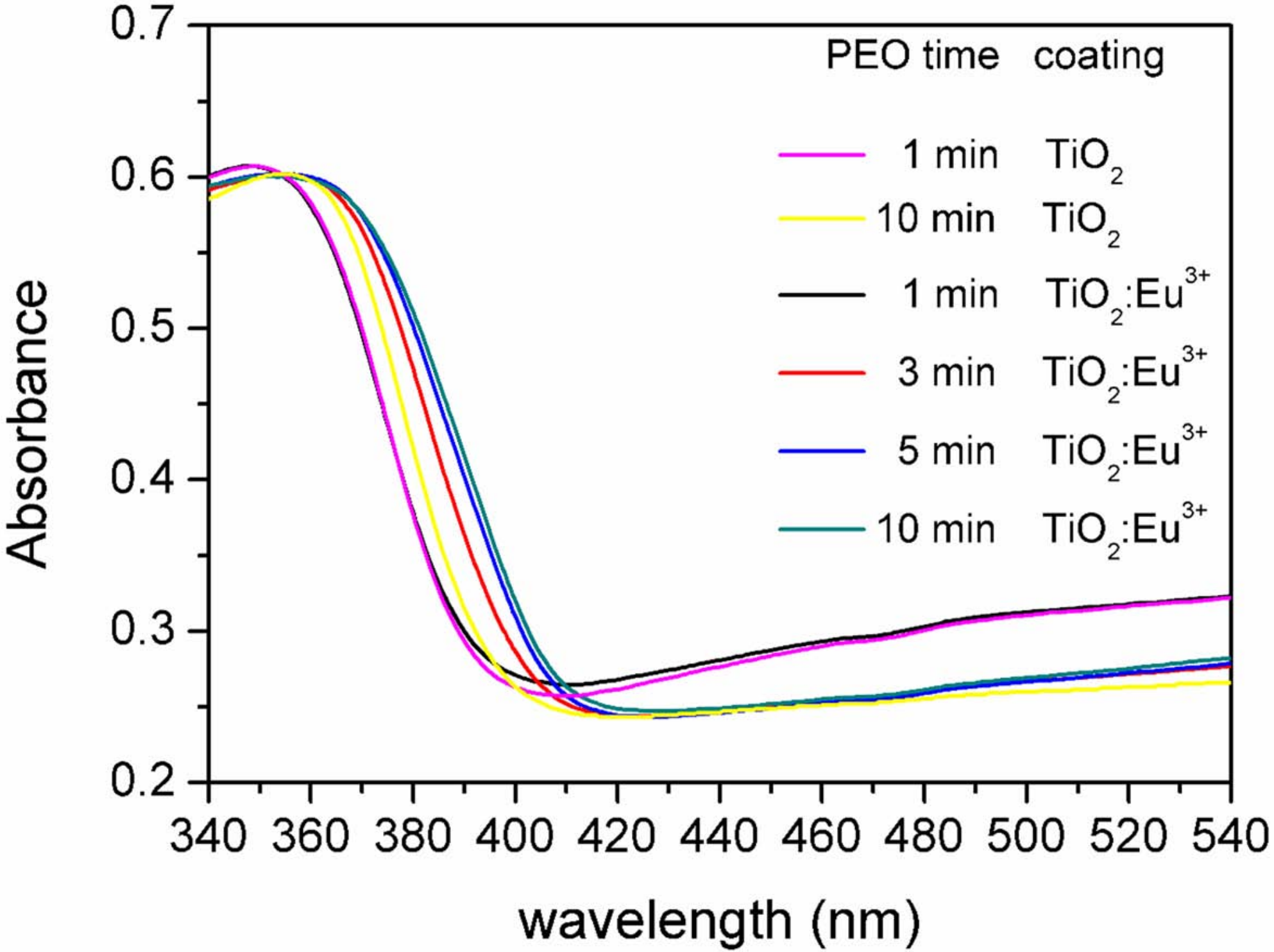
PEO time coating
1 min TiO2
10 min TiO2
1 min TiO2:Eu3+
3 min TiO2:Eu3+
5 min TiO2:Eu3+
10 min TiO2:Eu3+
Absorbance
0.7
0.6
0.5
0.4
0.3
0.2
340 360 380 400 420 440 460 480 500 520 540
wavelength (nm)

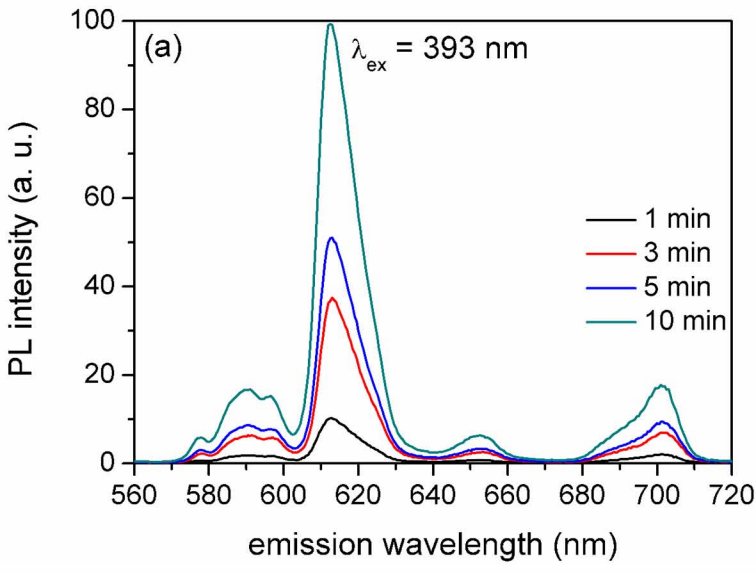
(a)
λ_{ex} = 393 nm
1 min
3 min
5 min
10 min
PL intensity (a. u.)
emission wavelength (nm)

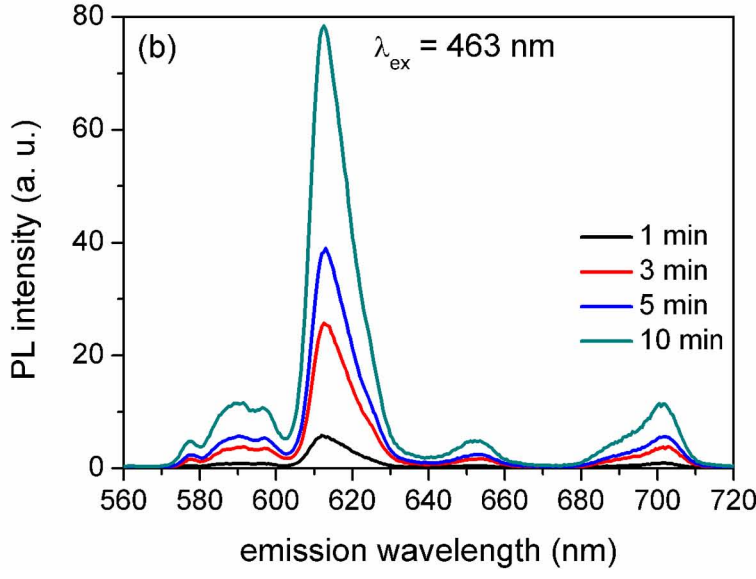
(b)
λ_{ex} = 463 nm
1 min
3 min
5 min
10 min
PL intensity (a. u.)
emission wavelength (nm)

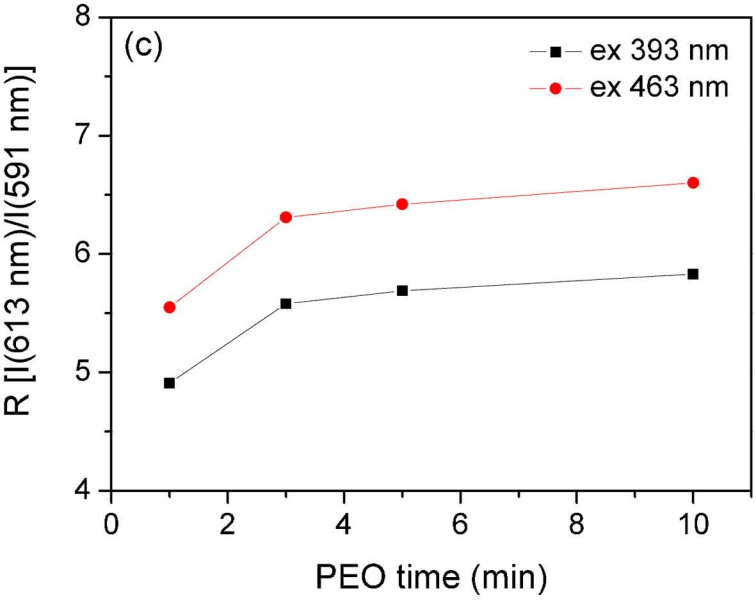
(c)
ex 393 nm
ex 463 nm
R [I(613 nm)/I(591 nm)]
PEO time (min)

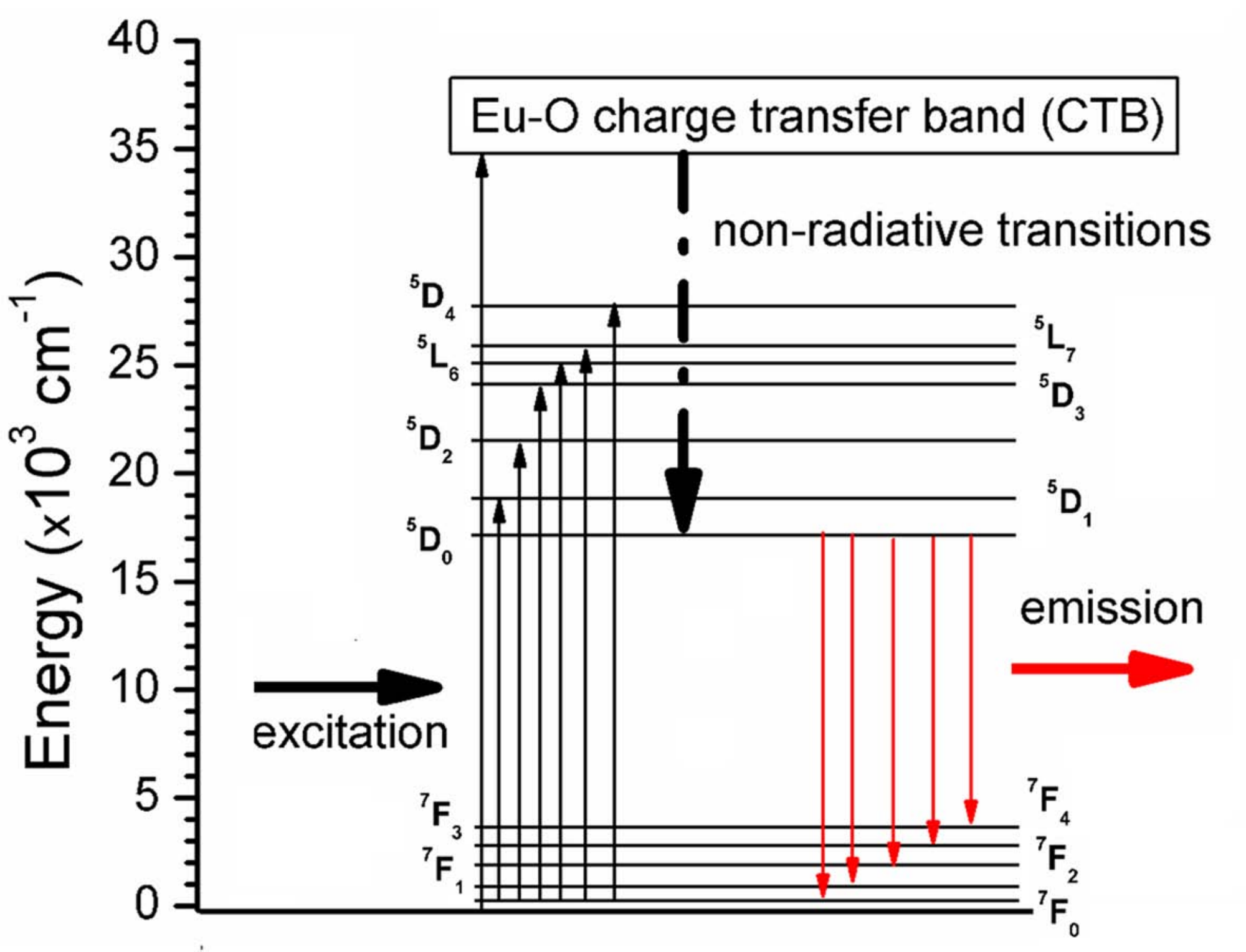
Energy (x10^3 cm^{-1})
40
35
30
25
20
15
10
5
0
Eu-O charge transfer band (CTB)
non-radiative transitions
$^5D_4$
$^5L_6$
$^5D_2$
$^5D_0$
$^5L_7$
$^5D_3$
$^5D_1$
emission
excitation
$^7F_3$
$^7F_1$
$^7F_4$
$^7F_2$
$^7F_0$

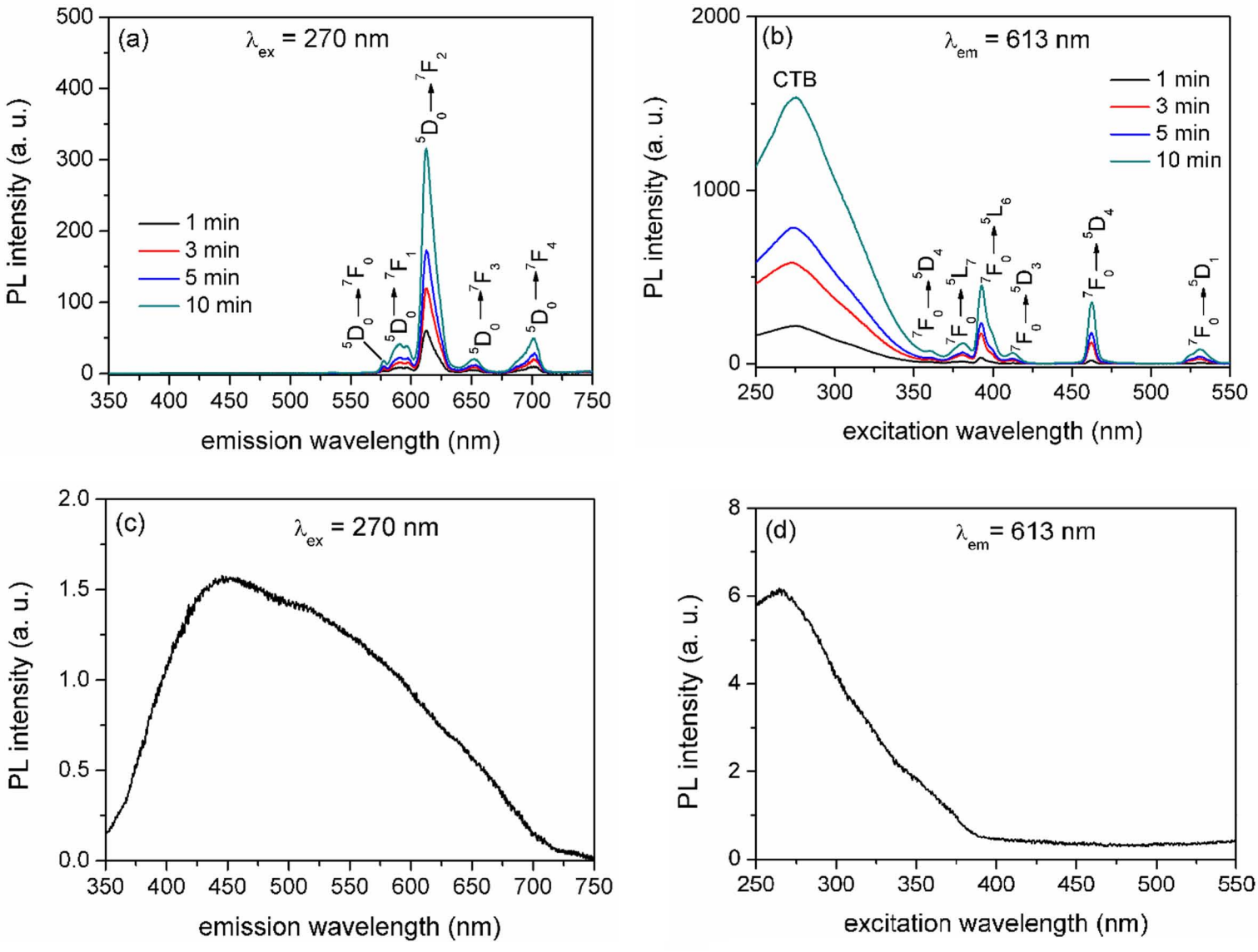
(a)
λex = 270 nm
PL intensity (a. u.)
emission wavelength (nm)
1 min
3 min
5 min
10 min
5D0→7F0
5D0→7F1
5D0→7F2
5D0→7F3
5D0→7F4
(b)
λem = 613 nm
CTB
PL intensity (a. u.)
excitation wavelength (nm)
1 min
3 min
5 min
10 min
7F0→5D4
7F0→5L7
7F0→5L6
7F0→5D3
7F0→5D4
7F0→5D1
(c)
λex = 270 nm
PL intensity (a. u.)
emission wavelength (nm)
(d)
λem = 613 nm
PL intensity (a. u.)
excitation wavelength (nm)

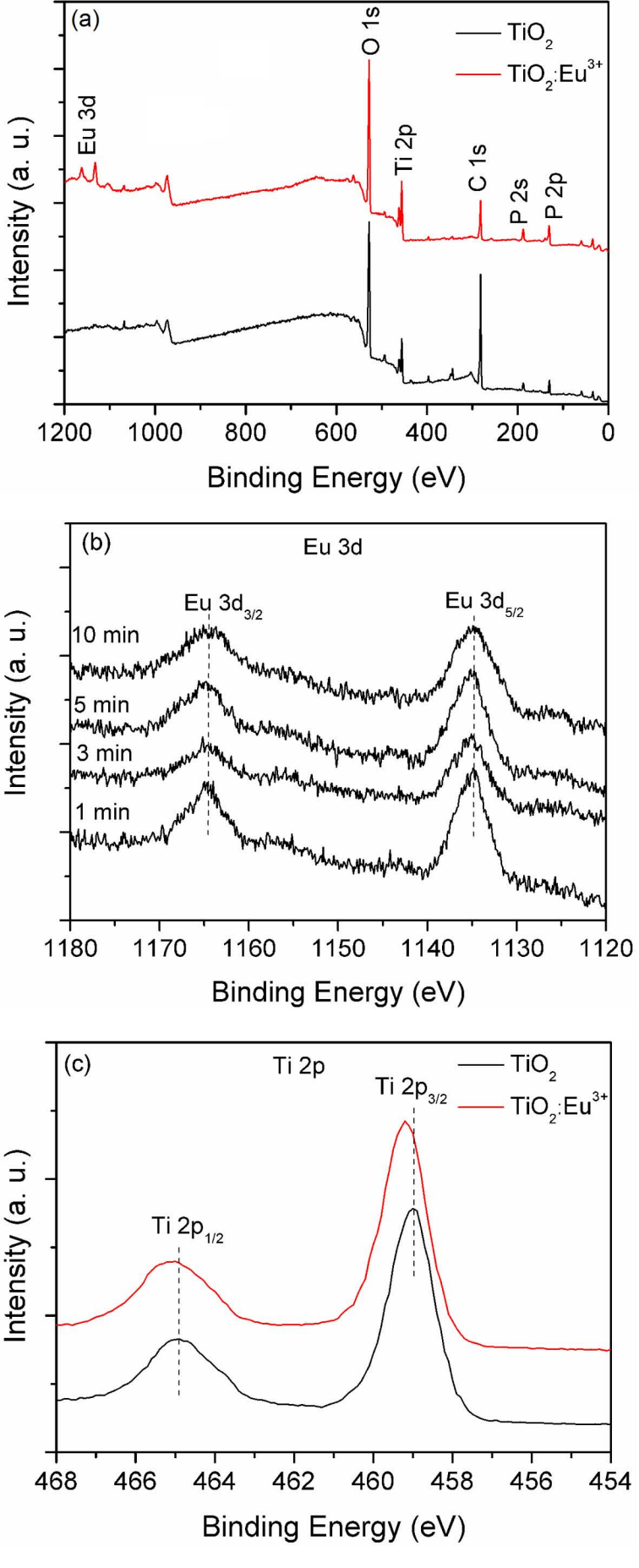
(a)
TiO2
TiO2:Eu3+
O 1s
Eu 3d
Ti 2p
C 1s
P 2s
P 2p
Intensity (a. u.)
1200
1000
800
600
400
200
0
Binding Energy (eV)
(b)
Eu 3d
Eu 3d3/2
Eu 3d5/2
10 min
5 min
3 min
1 min
Intensity (a. u.)
1180
1170
1160
1150
1140
1130
1120
Binding Energy (eV)
(c)
Ti 2p
TiO2
TiO2:Eu3+
Ti 2p3/2
Ti 2p1/2
Intensity (a. u.)
468
466
464
462
460
458
456
454
Binding Energy (eV)

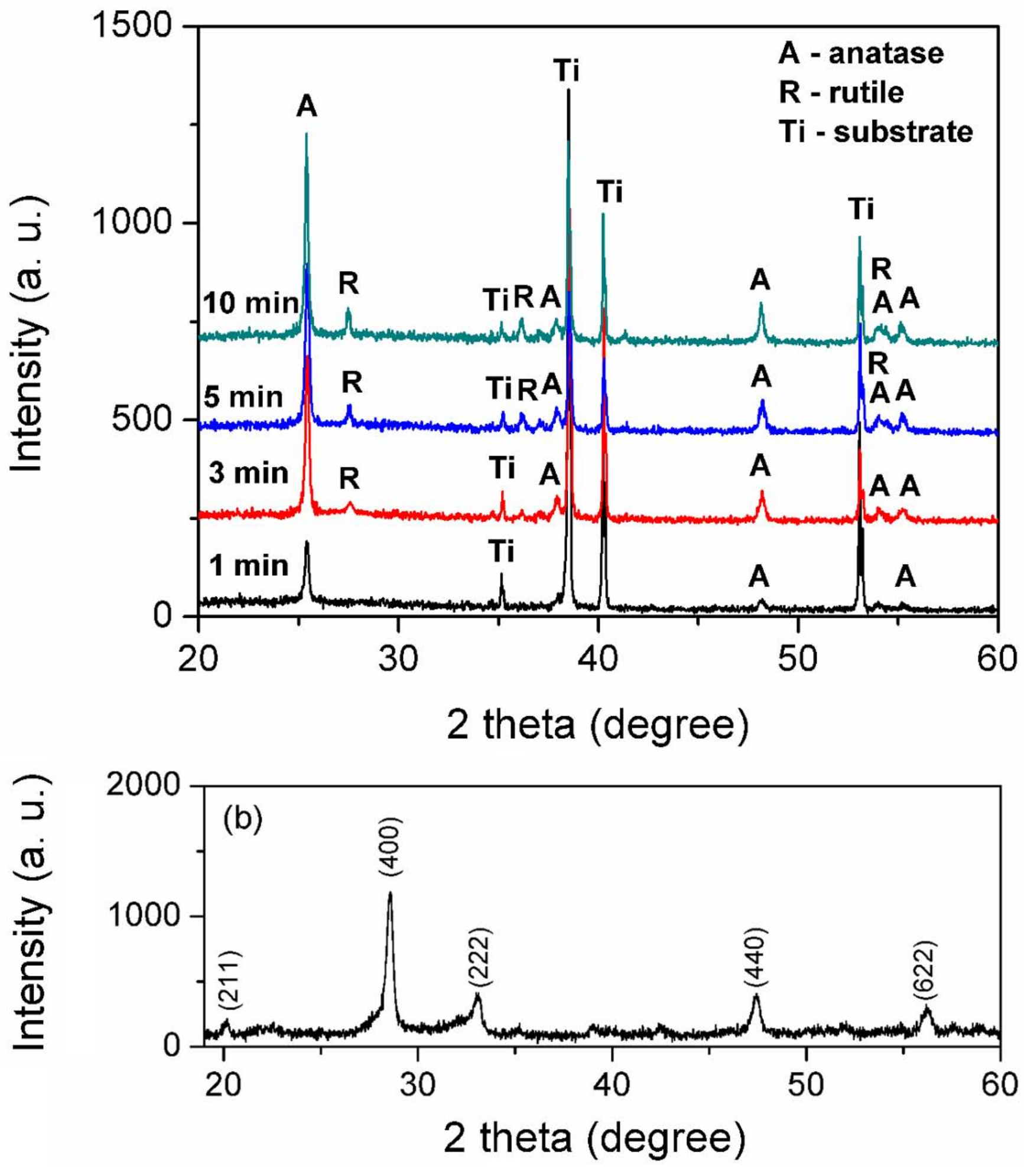
A - anatase
R - rutile
Ti - substrate
10 min
5 min
3 min
1 min
Intensity (a. u.)
2 theta (degree)
(b)
(211)
(400)
(222)
(440)
(622)

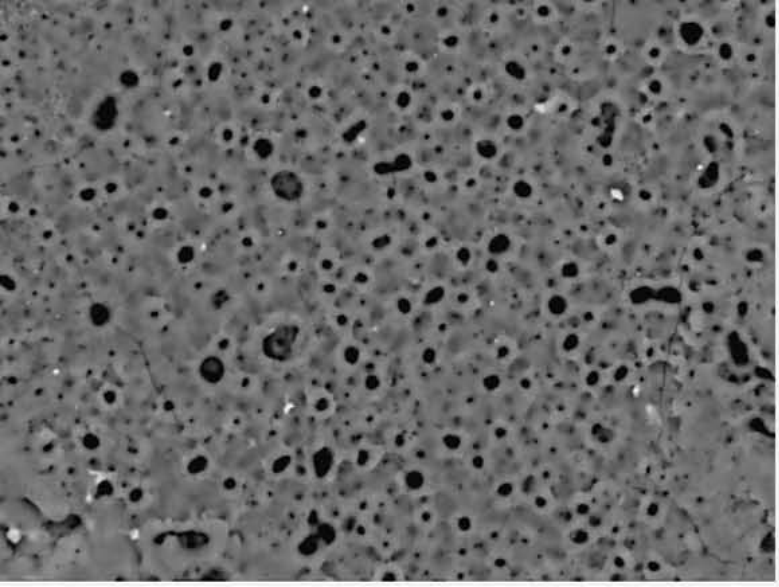
60 μm

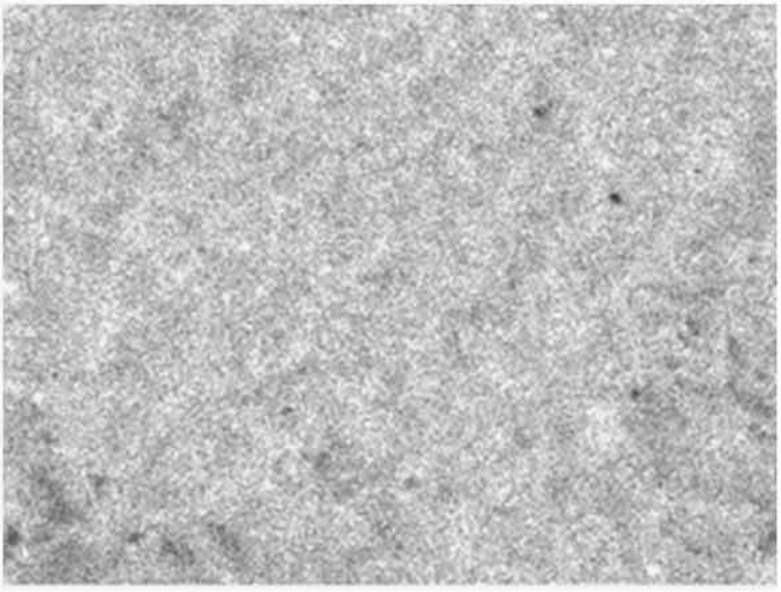
60 μm
Ti

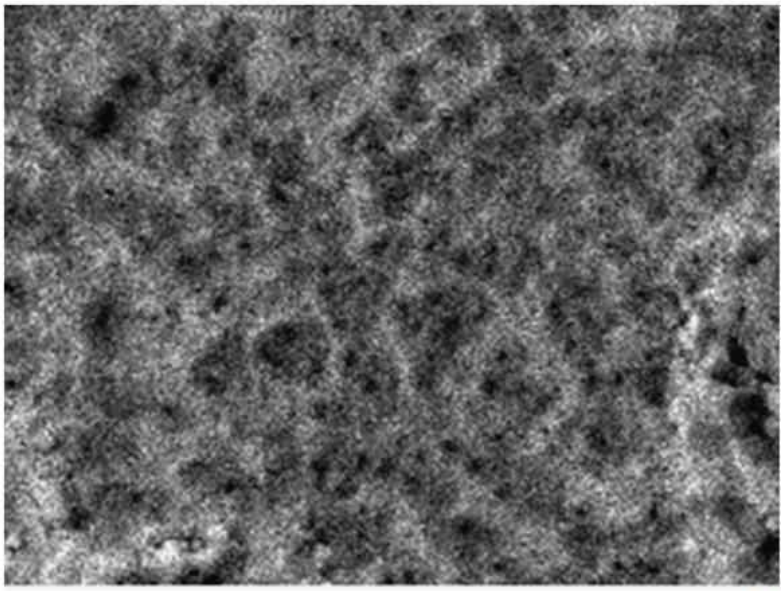
60 μm
P

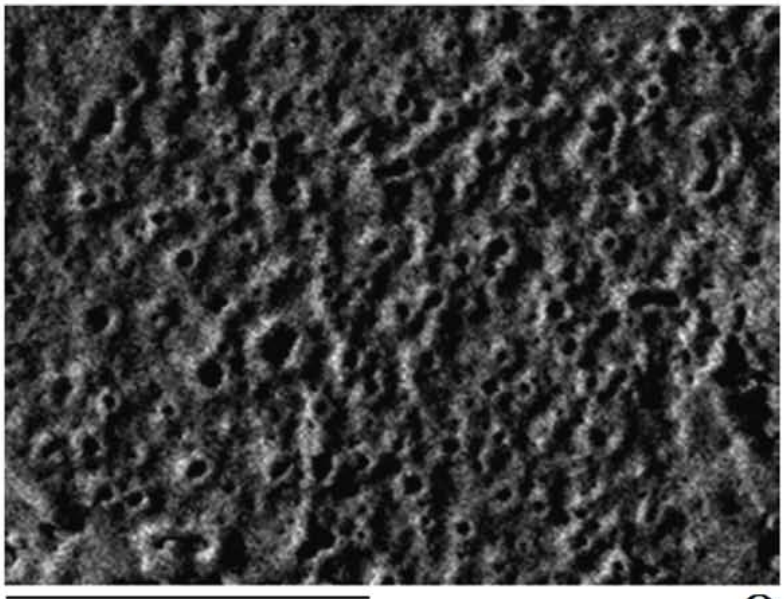
60 μm
O

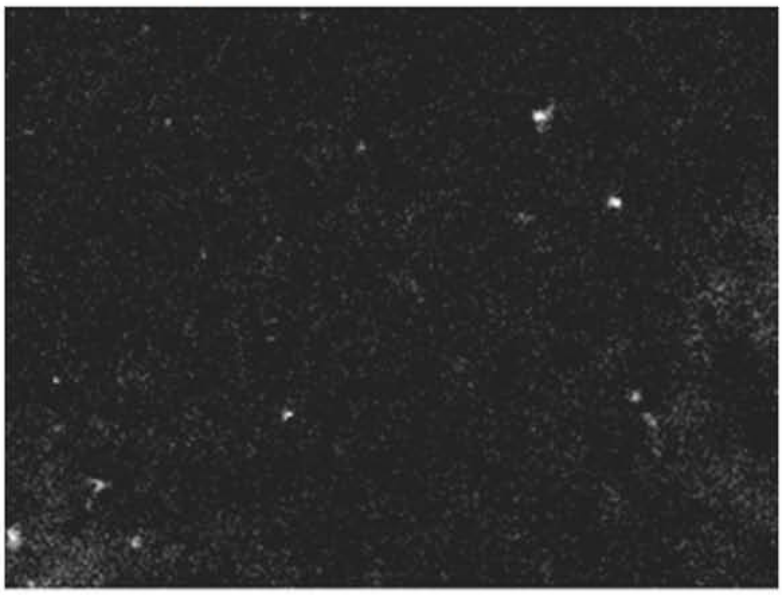
60 μm
Eu

(a)

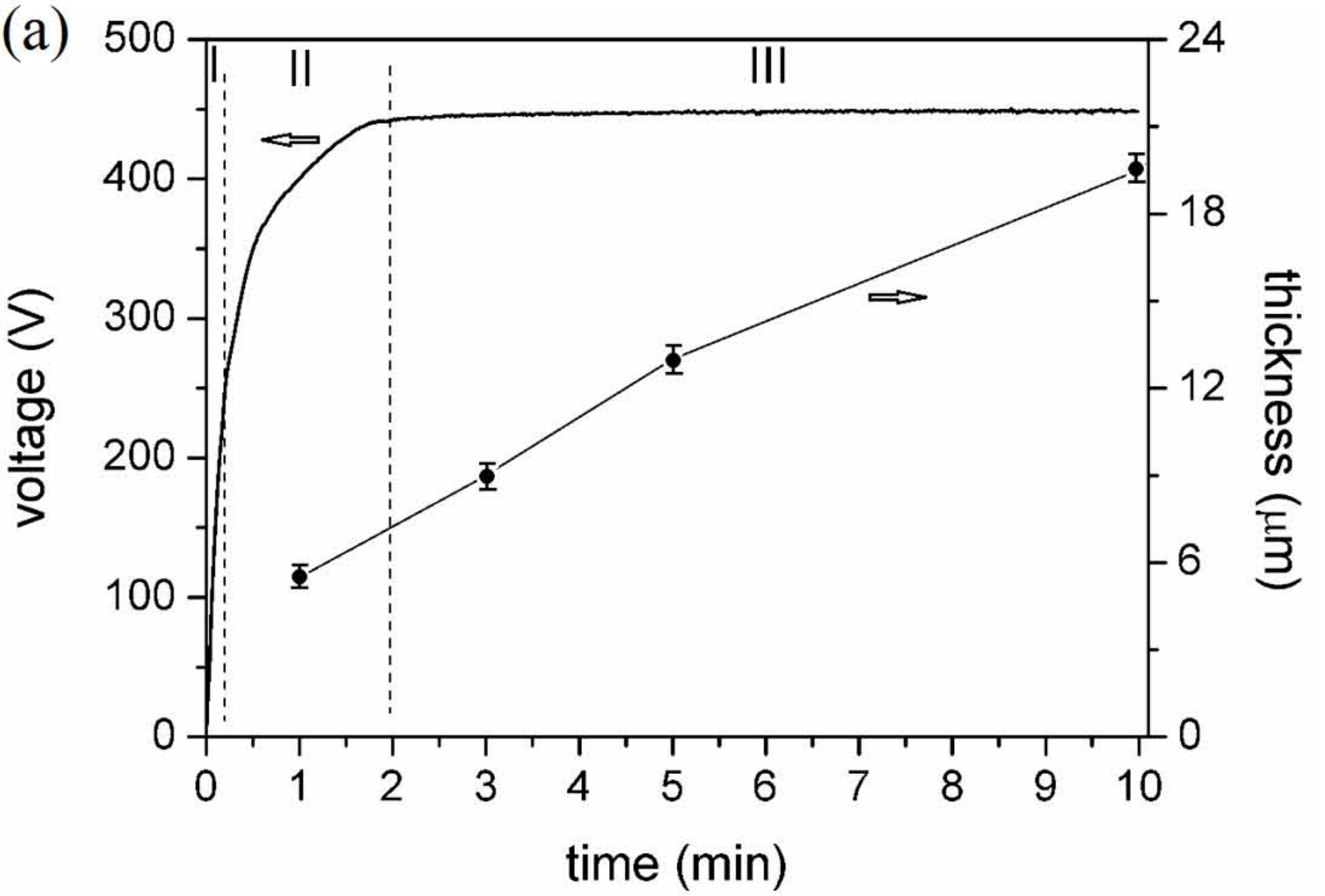
I
II
III
voltage (V)
thickness (μm)
time (min)
0
100
200
300
400
500
0
6
12
18
24
0
1
2
3
4
5
6
7
8
9
10

(b)

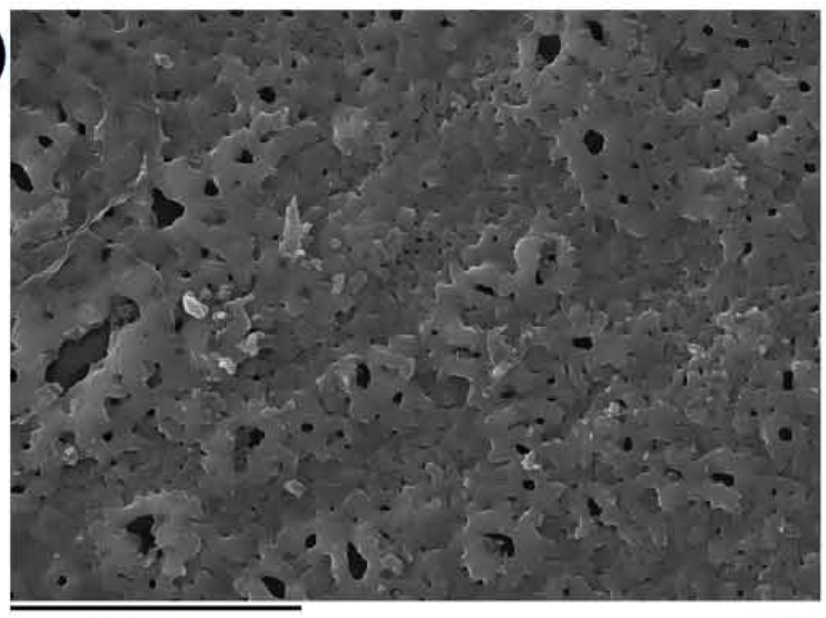
20 μm
(i)

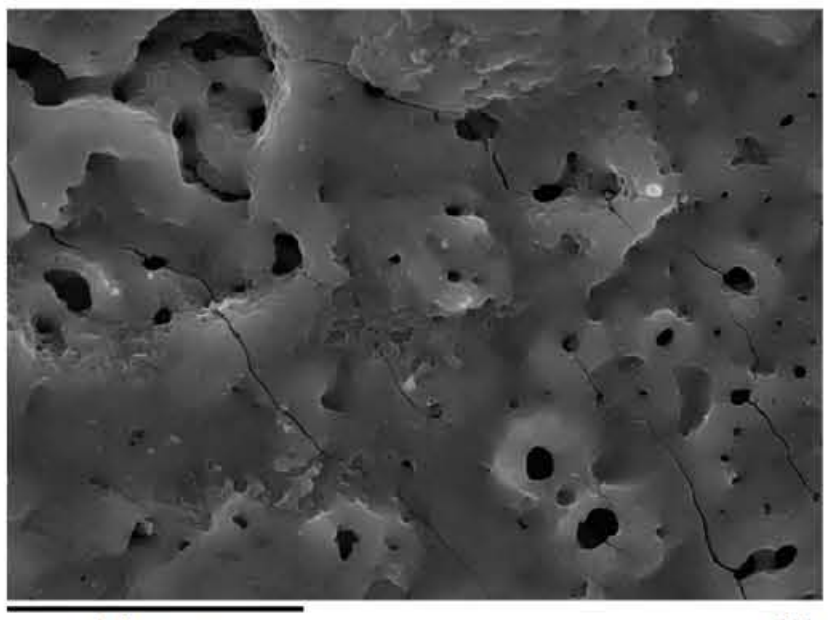
20 μm
(ii)

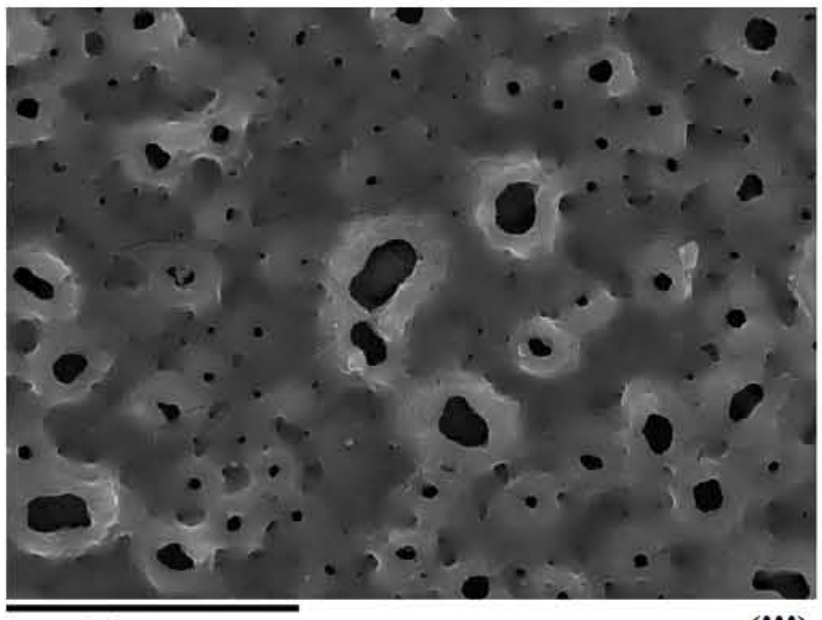
20 μm
(iii)

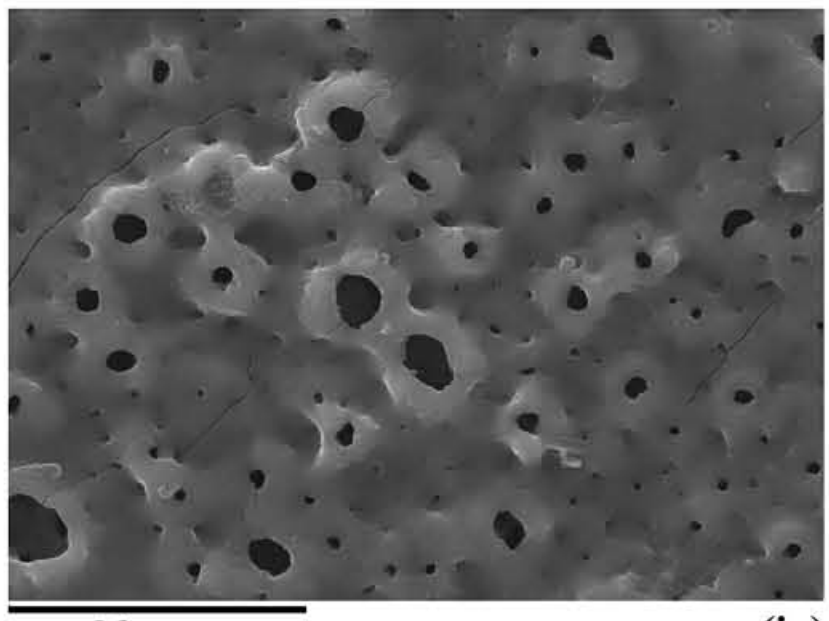
20 μm
(iv)

(c)

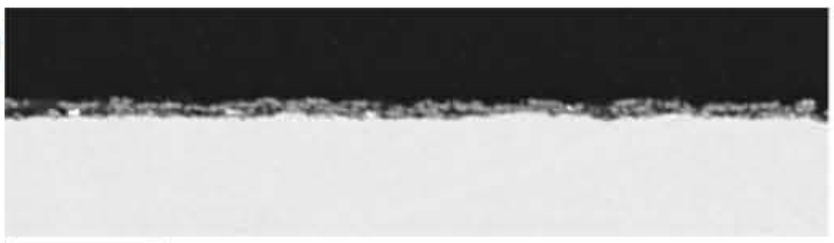
50 μm
(i)

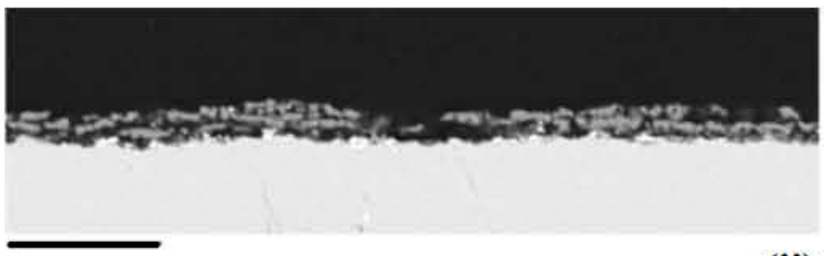
50 μm
(ii)

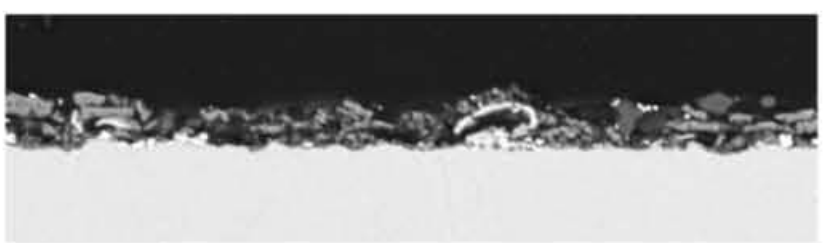
50 μm
(iii)

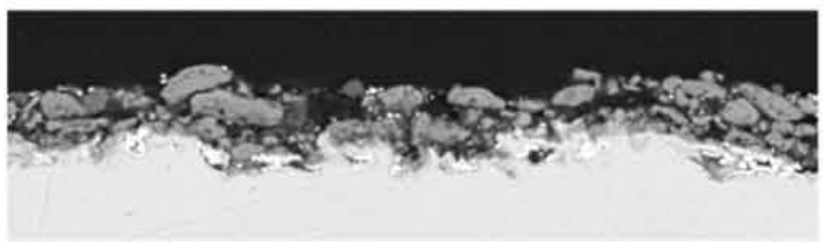
50 μm
(iv)

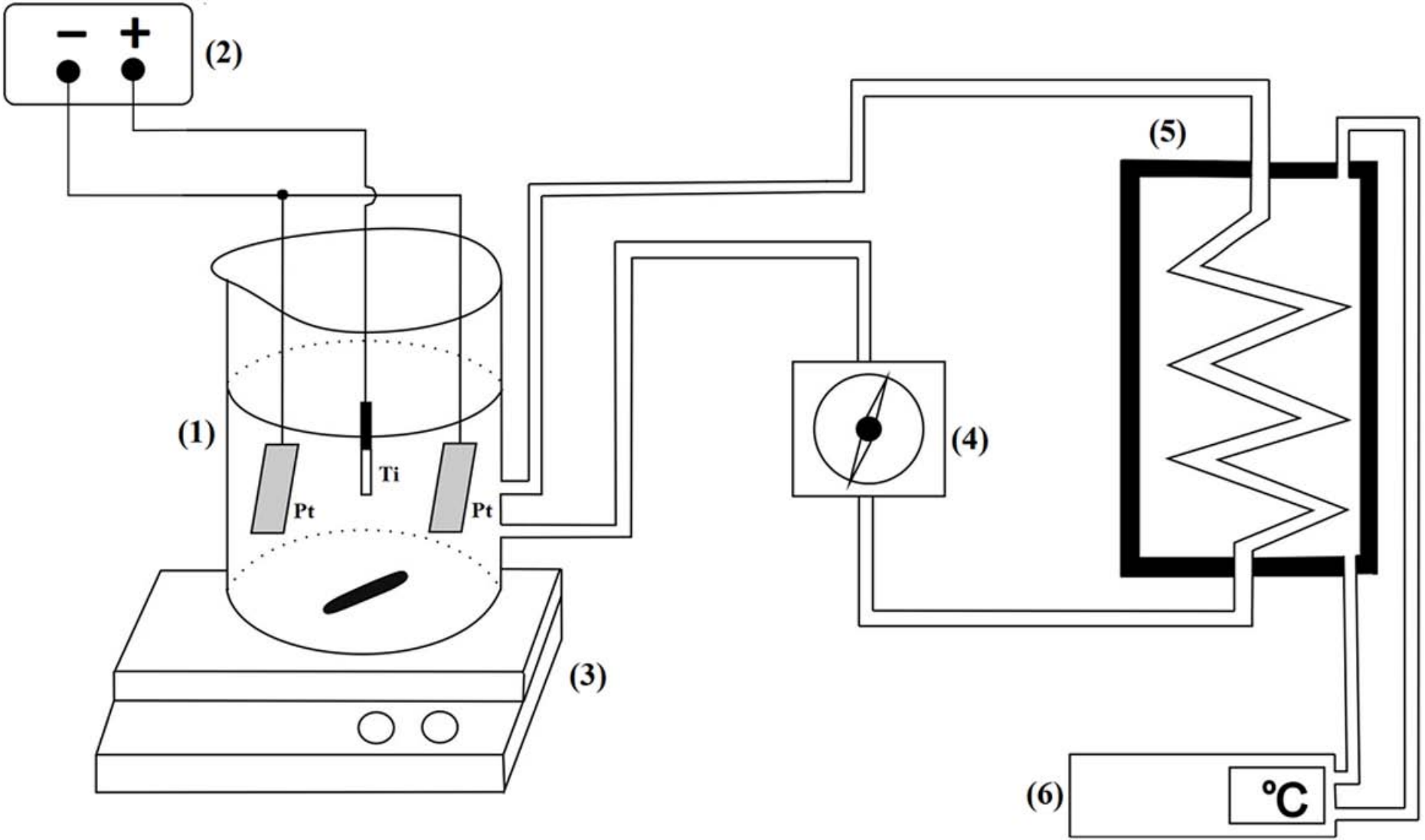
(2)
(1)
Ti
Pt
Pt
(3)
(4)
(5)
(6)
°C